Acoustic emission characteristics during the microcracking processes of granite, marble and sandstone under mode I loading

Tian Yang Guo, Qi Zhao*

Department of Civil and Environmental Engineering, The Hong Kong Polytechnic University, Hong Kong, China

*Correspondence to: Qi Zhao (qi.qz.zhao@polyu.edu.hk)

Abstract: We conduct a comparative laboratory investigation of the cracking behaviour of granite, marble and sandstone using semi-circular bending (SCB) tests on pre-notched specimens with acoustic emission (AE) monitored. We analyze and compare the spatial-temporal evolution, relative amplitude, and source mechanisms of the AE events. To explain the differences in the AE characteristics, we examine the microscopic features of macrocracks induced in the SCB tests using the thin-section petrographic analysis. We find that the temporal evolution patterns of AE events are generally similar among the three rocks. Most AE events are observed in the granite and the least in the sandstone. The AEs in the granite and marble both concentrate near the notch tip, while those in the sandstone distribute along the macrocrack path. The AEs in the granite and marble may be mainly attributed to the reactivation of pre-existing microcracks near the notch tip. The AEs in the sandstone could be more induced by the nucleation of new microcracks in the area where the macrocrack would subsequently form. For all three rocks, the tensile events are the predominant event type. Much more shear events are observed in the granite as compared with the marble and sandstone. These differences in the quantity, distribution and source mechanisms of AE events are related to the distinct microstructural characteristics of the three rocks. Our results provide valuable insights into the understanding of the correlation between rock microscopic features and characteristics of AE activities that may facilitate more rigorous AE analysis in rock engineering practice.

Highlights:

- The amount of acoustic emission events is closely related to the number of pre-existing microcracks.
- The distribution pattern of acoustic emission events varies with rock type in mode I semi-circular bending tests.
- Much more shear acoustic emission events are observed in the granite than the marble and sandstone.

Keywords: Acoustic emission, Static semi-circular bending, Microcracking mechanisms, Mode I loading, Fracture process zone

1 Introduction

Studying the cracking behaviour of rocks is important in the design, construction, and operation of rock engineering projects such as rock slope construction, tunnel excavation, and geothermal energy exploitation. For example, the potential failure surface formed during the initiation and coalescence of different scales of cracks could affect the stability of rock slopes (Huang, 2007). During the tunneling in deep-buried brittle rocks, rockburst is a commonly encountered geological disaster that is closely related to the formation of macrocracks (Feng, 2017). In enhanced geothermal systems, hydraulic fracturing is widely used to create fracture networks to increase the productivity of the geothermal reservoir (Olasolo et al., 2016). Therefore, having a good understanding of the cracking behaviour of rocks could contribute to evaluating the safety and optimizing the performance of rock engineering projects.

Apart from the field investigation and numerical simulation, the laboratory experiment is one of the important methods to study the cracking behaviour of rocks under controlled conditions. Previous experimental studies reveal that before the initiation of a macrocrack under loading, a number of microcracks with widths smaller than mineral grain size form in a region near the macrocrack tip known as the fracture process zone (FPZ) in which the rock behaves inelastically (Friedman et al., 1972; Labuz et al., 1987; Whittaker et al. 1992). The macrocracks and microcracks are defined as the cracks with an order of magnitude of cm and μm in scale, respectively (Li & Einstein, 2017). As the load increases, more microcracks nucleate and grow in the FPZ until the microcrack density reaches a critical value, and the FPZ at this moment is defined as the fully-developed FPZ (FD-FPZ) (Ashby & Hallam, 1986; Tal

et al., 2016). Then, the macrocrack extends by linking the adjacent microcracks ahead of the crack tip. The development of these microcracks which is defined as microcracking behaviour in this study can be the precursors of the formation of the macrocrack. In addition, the FPZ features are of potential importance for certain geotechnical engineering projects such as enhanced geothermal systems where the enhancement of reservoir permeability is a key issue, as the FPZs have enhanced permeability (Chandler et al., 2018). Therefore, it is important to conduct comprehensive and systematic investigations on the microcracking behaviour of rocks.

Acoustic emissions (AEs) are defined as transient elastic waves caused by the rapid energy release from localized sources within a material (ASTM E1316-21). The development of microcracks in rocks is accompanied by the radiation of AEs (Lockner 1991; Lockner, 1993). The AE technique is one of the robust and powerful tools to monitor and investigate the microcracking process in rock fracturing tests. Based on the detected AE signals, the AE characteristics such as AE signal parameters (count, hit, event, amplitude, energy) (Chen et al., 2021; Meng et al., 2020; Wang et al., 2020; Yao et al., 2020; Zhang et al., 2021), locations (Li et al., 2021; Meng et al., 2019; Zhao & Glaser, 2020), relative energy (Meng et al., 2018; Zheng et al., 2020) and source mechanisms (Li & Einstein, 2017; Kong et al., 2021; Guo & Wong, 2021) of AE events can be analyzed. These AE characteristics could advance our understanding of the microcracking behaviour of rocks.

In rock fracture mechanics, the loading applied to a crack tip can be generally classified into three basic modes, namely, mode I (tension), mode II (the in-plane shear) and mode III (out-of-plane shear) according to the loading configuration (Whittaker et al., 1992). Because rocks are relatively weak in tension, the cracking behaviour of rocks under quasi-static mode I

loading attracts substantial attention in the rock fracture mechanics community. Although a number of theoretical models were proposed to describe the sizes and shapes of FPZs in rocks under quasi-static mode I loading (Barenblatt et al. 1959; Dugdale 1960; Irwin, 1997; Labuz et al., 1985; Schmidt 1980), all these models are based on assumptions that the materials are homogenous which may deviate from the actual behaviour of rocks in FPZ (Whittaker et al., 1992), especially with the presence of microscale features such as mineral heterogeneity and microcracks. In view of this, a large number of researchers experimentally investigated the microcracking processes of various rocks under quasi-static mode I loading using the AE technique (Table 1). In these studies, the AE event clusters are presented to visualize the sizes and shapes of the FPZs. The spatial-temporal evolution of AE events has been investigated to understand the development of microcracks or FPZs. Besides, more valuable information related to microcracking mechanisms can be extracted from the AE parameters such as AE amplitude and source mechanisms. The previous studies have demonstrated that the textural properties (e.g. grain size and pre-existing microcracks) of granite significantly affect their microcracking behaviour and associated AE characteristics (Guo & Wong, 2020, Guo et al., 2021). It is interesting and necessary to have a comprehensive and systematic study on the AE characteristics of different rock types with various textural properties which describe the size, shape, and arrangement of the grains (for sedimentary rocks) or crystals (for igneous and metamorphic rocks). However, most of the previous studies focus on one type of rock in each test, only a few have conducted comparison studies on the AE characteristics of some rocks such as granite, limestone, sandstone and shale (Hoagland et al., 1973; Labuz & Biolzi,1998; Li & Einstein, 2019). Moreover, the microcracking mechanisms causing the distinct AE

characteristics of different rock types have been seldom explored.

To fill in the gap, we conduct a comparative experimental study on the AE characteristics induced by the development of microcracks prior to the initiation of a macrocrack under mode I loading in commonly seen igneous, metamorphic and sedimentary rocks. The rocks we use are Miluo granite, Sichuan marble, Yunan red sandstone, and they are referred to as granite, marble, and sandstone in this manuscript, respectively. The static mode I three-point bending tests are conducted on the semi-circular bend specimens made from the three rocks with AE monitored. We analyze and compare the spatial-temporal evolution, relative amplitude and source mechanisms of AE events. To explain the differences in AE characteristics among the three rocks from the microscopic perspective, we conduct microscopic observation on the thin-section sample containing the marcocracks induced in the SCB tests using a petrographic microscope.

2 Materials and Methods

2.1 Material and specimen preparation

The granite consists of 33 % quartz, 35 % K-feldspar, 29 % plagioclase and 3 % biotite with grain sizes ranging from 0.23 mm to 1.98 mm and the average grain size is 0.81 mm. The marble consists of 74 % dolomite and 26 % calcite. Its grain size ranges from 0.09 mm to 0.19 mm with a mean value of 0.36 mm. The sandstone is composed of around 49 % quartz, 13 % K-feldspar, 29 % plagioclase, 4 % perilla pyroxene and 5% hematite, which has a grain size ranging from 0.03 mm to 0.14 mm with a mean value of 0.09 mm. The porosity of the granite,

marble and sandstone are 0.37 %, 0.18 % and 1.45 %, respectively, measured according to the International Society for Rock Mechanics and Rock Engineering suggested method for porosity determination (Ulusay & Hudson, 2007). The mean P wave velocity (V_p) of the granite, marble and sandstone are 4071 m/s, 4714 m/s and 2883 m/s, respectively. Measured V_p values are within the ±5%, ±6% and ±1% of the mean V_p for the granite, marble and sandstone, respectively. The V_p of the specimens are measured from different directions, thus, the specimens tested in this study are considered isotropic, and the mean V_p values are used for AE location.

The representative thin-section photos of the granite, marble, and sandstone under cross-polarized light (XPL) are shown in Fig. 1. The typical interlocking texture is observed in the granite where a number of microcracks are observed in quartz grains (Fig. 1a). The marble is characterized by the interlocking polygonal texture (Fig. 1b). There are relatively fewer microcracks in the mineral grains of the marble as compared with the granite. The sandstone consists of well-sorted fine grains (Fig. 1c). A zoom-in view of the grains of the sandstone under plane-polarized light (PPL) shows that few microcracks can be observed in the grains (Fig. 1d). In summary, the granite and marble are strongly and slightly fissured nonporous rocks, respectively, and the sandstone is a nonfissured porous rock.

The semi-circular bend (SCB) specimen is a semi-circular specimen with a straight-through central notch (Fig. 2b) (Lee et al., 2015). The specimens were prepared according to the procedures described in Wong et al. (2019). The radius (R) and thickness (B) of the SCB specimens are designed to be 50 mm and 40 mm respectively. The width (t) and length (a) of the notch are 0.7 mm and 21 mm, respectively. To avoid the potential effect of the rock

anisotropy on its microcracking behaviour, the notches are elaborately designed to align along the same direction for all the SCB specimens for each rock type.

2.2 Semi-circular bending (SCB) test

In the static SCB test, the SCB specimens are subjected to symmetric three-point bending with the span distance 2*S* of 50 mm (in Fig. 2b) until macrocracks that fail the specimen form. The thin notch of the specimen in the SCB test can simulate the behaviour of an open macrocrack under mode I loading. The SCB tests have been widely used to measure the static mode I fracture toughness (K_{IC}) of rocks (Chang et al., 2002; Funatsu et al., 2015; Guo et al., 2021; Kataoka et al., 2015; Kuruppu et al., 2014; Lee et al., 2015; Mahanta et al., 2016; Tutluoglu & Keles, 2011; Wei et al., 2016b, 2017, 2021; Wong & Guo, 2019; Wong et al., 2019). The K_{IC} can be calculated based on the peak load, P_{max} and the geometric parameters of the SCB specimen (Kuruppu et al., 2014):

$$K_{IC} = Y' \frac{P_{\max}\sqrt{\pi a}}{2RB} \tag{1}$$

$$Y' = -1.297 + 9.516(S/R) - \left(0.47 + 16.457(S/R)\right)\beta + \left(1.071 + 34.401(S/R)\right)\beta^2 \tag{2}$$

where $\beta = a/R$, and Y' is the critical stress intensity factor.

In this study, we conduct the SCB tests on four, five and five SCB specimens for the granite, marble and sandstone, respectively. The SCB tests are conducted on the VJ Tech TriSCAN 100 kN load frame in the displacement control mode at the rate of 0.05 mm/min. This displacement control mode allows us to study the AEs induced by microcracking prior to the formation of the macrocrack, which is different from the crack-opening-based loading

control in studies of Li et al. (2015) and Li & Einstein (, 2017) where the AEs both before and after the macrocrack initiation are investigated. The applied axial load and displacement are measured using TCLP-NB load cell and CDP-25 displacement transducer which are logged using the UCAM-60 series data logger every 1.5 s. The loading test is terminated when a drastic drop of the axial load is observed.

2.3 Acoustic emission (AE) measurement

The Physical Acoustics Corporation (PAC) AE system consists of four pieces of PCI-2 boards with totally eight channels, eight 2/4/6 preamplifiers and eight AE PICO sensors. The AE PICO sensor is cylindrical with 5 mm in diameter and 4 mm in height. It is a resonant-type sensor, which has clear peak sensitivity around its resonant frequency of 500 kHz. The operating frequency of this sensor ranges from 200 to 750 kHz. Eight AE sensors are attached to the front and back surfaces of the SCB specimen using the Aron Alpha Instant Glue (Fig. 2a). The AE sensors (Fig. 2c) are arranged to have good spatial coverage of the notch tip for better location accuracy. The AE waveforms are first amplified by 40 dB using the preamplifier and then recorded at 10 MHz frequency and digitized at 16-bits resolution. The AE waveforms are recorded with triggered mode with an amplitude threshold of 45 dB. The AE time parameters are set as: Peak Definition Time = 200 μs, Hit Definition Time = 800 μs, Hit Lockout Time = 1000 μs. The software AEwin for PCI2 is used to output the AE waveforms. Pencil lead break tests are conducted on each specimen before the SCB test by breaking 0.5-mm-diameter pencil leads at a known location (P1 in Fig. 2c) three times. The objectives of the pencil lead break test are twofold: (1) to check the operation condition of the entire system; (2)

to check the AE location accuracy.

The waveforms collected during the SCB tests are then processed following the algorithms: the first arrival of the P wave is automatically picked by the Akaike Information Criterion (AIC) picker (Akaike 1998, Carpinteri et al., 2012). The AE event localization is conducted using Geiger's method (Geiger 1910; 1912) with a constant P wave velocity. The location accuracy estimated from the pencil lead break tests are 8.0 mm, 4.0 mm and 4.4 mm for the granite, marble sandstone, respectively.

The relative amplitude (hereinafter called amplitude for short) of an AE event, is calculated using the equation (Kwiatek et al., 2014): $E_{\mathrm{AE}} = (\frac{1}{n}\sum_{i=1}^{n}(A_i R_i)^2)^{0.5}$, where A_{i} (unit: V) is the first peak of the P wave of the AE waveform for sensor *i*. R_{i} (unit: mm) is the distance between an AE event and sensor *i*. Note that we use the relative amplitude here to avoid confusion with the absolute magnitude scales used in seismology. To evaluate the source mechanisms of an AE event, a number of methods have been proposed such as simplified Green's function for moment tensor analysis (SiGMA) method (Ohtsu, 1991; 1995) and the polarity pattern method (Zang et al., 1998). As compared with the SiGMA method, the polarity pattern method required fewer input parameters and can provide adequate source mechanism information (Graham et al., 2010). In this study, we analyze the source mechanisms based on the polarity pattern method. The average polarities (*pol*) of the first peaks of P waves (A_i) of the AE waveforms used to locate the AE event can be calculated using the equation (Zang et al., 1998): $pol = \frac{1}{n}\sum_{\mathrm{i=1}}^{n}\mathrm{sign}(A_i)$. The AE events can be divided into tensile ($-1 \le pol < -0.25$), shear ($-0.25 \le pol \le 0.25$) and collapse ($0.25 < pol \le 1$) according to the *pol* value (See

examples in Fig. S1 in the supplementary material).

2.4 Thin-section petrographic analysis

To better explain the AE characteristics during the microcracking processes of different rocks, we conduct microscopic analysis on the thin-section samples containing the macrocracks induced in the SCB tests using a petrographic microscope. The failed SCB specimens are carefully preserved after the SCB test, and the thin-section samples are prepared following the procedures below:

(1) The fracture surfaces of the SCB specimens are glued with the Epo-Tek 301 Epoxy. The SCB specimens will then be placed in an oven with 60 ℃ for 24 hours for curing.

(2) We then cut the small pieces of cuboid samples containing the macrocracks with the dimensions of around 35 mm (length) × 2.5 mm (width) × 5 mm (thickness) from the central section of the SCB specimens (Fig. 3).

(3) Then, standard thin-section samples with 0.03 mm thickness are prepared from the cuboid samples.

The thin-section samples are examined under XPL and PPL using a Nikon Eclipse 50i POL microscope with an amplification factor of 10 for the eyepiece. The amplification factor for the objective will be adjusted during the examination according to the rock type. The digital photos of the thin-section samples are captured by a Nikon DF-Ri2 camera equipped on the microscope.

3 Results

3.1 Load-displacement behaviour

The typical axial load versus displacement curves of the granite, marble and sandstone are presented in Fig. 4a. The shapes of the curves are similar for the three rock types. The load first increases nonlinearly with the displacement when the load level is low. The curves then become linear as the load level increases. The curves become non-linear with the slopes decreasing when approaching the peak load, P_{max}. Then, the load drops rapidly after the peak at the failure of the specimen. The marble specimens have the largest average P_{max} of 2387.6 N, while the sandstone has the smallest average P_{max} of 1230.6 N (Fig. 4b). The mean P_{max} of the granite is slightly lower than that of marble at 2180.2 N. The P_{max} values of the five SCB marble specimens are the most scattered, while those of the five SCB sandstone specimens are the least scattered. The mean K_{IC} values of the granite, marble and sandstone are measured to be 0.47, 0.50 and 0.27 MPa·m$^{0.5}$, respectively. The K_{IC} values of the five SCB marble specimens are the most scattered, while those of the five SCB sandstone specimens are the least scattered (Fig. 4c).

3.2 AE results

3.2.1 Spatial-temporal evolution of AE events

According to the variations of AE event rate with the normalized displacement of all the tested granite (Fig. 5a), marble (Fig. 5b) and sandstone (Fig. 5c) specimens, the representative temporal evolution of AE events of the three types of rocks are presented (Fig. 5d, e, f). The temporal evolution patterns of AE events are generally similar among the granite (Fig. 5d),

marble (Fig. 5e) and sandstone specimens (Fig. 5f): Few AE events are detected at the beginning of the test as the axial load is low. As the load reaches a high level and increases linearly with displacement, a few AE events appear. The AE event rate keeps almost constant and below 10 /s (slow AE development phase). As the load further increases and approaches its peak, the AE event rate increases exponentially indicating the rapid increase of AE events (Fig. 5d, e, f), which is commonly observed in some AE studies (Li et al., 2019). The AE event rate reaches its maximum following by a quick decrease at the end of the test.

Under the same loading rate of 0.05 mm/min, the total period with AE activities is the longest for the granite specimen at ~84s (Fig. 5d) and the shortest for the sandstone specimen at ~12 s (Fig. 5e). For all the tested specimens, the maximum AE event rate is the largest for the granite and the smallest for the sandstone (Fig. 6a). The mean values of the maximum AE event rate of the granite, marble and sandstone are 112/s, 44/s and 42/s, respectively. The difference in the duration of the AE development phases and maximum AE event rate results in the distinct cumulative AE event number preceding the initiation of macrocracks. The granite specimens have much larger cumulative AE event numbers as compared with those of marble and sandstone specimens (Fig. 6b). The average values of the cumulative AE event numbers of the granite, marble and sandstone are 1345, 234 and 79, respectively.

The granite (Fig. 7a) and marble (Fig. 7b) specimens have similar spatial-temporal evolution features of AE events: At the beginning of the slow AE development phase, a few AE events scatter around the notch tip. As the load increases, more AE events are detected and most of them cumulate near the notch tip. As it enters the fast AE development phase, the number of AE events increases exponentially and the AE events mainly distribute within a

narrow band area, and the event cluster is generally symmetric to the central notch plane. The AE events are observed both ahead of and behind the notch tip. However, the spatial-temporal evolution characteristics of the AE events of the sandstone specimen (Fig. 7c) are different from the granite and marble. At the beginning of the slow AE development phase, a number of AE events concentrate around the notch tip. During the fast AE development phase, more AE events appear gradually far away from the notch tip and along the propagation direction of the macroscopic crack. In the sandstone, most of the AE events distribute ahead of the notch tip.

The cumulative AE events at the end of the fast AE development phase provide important information on the FD-FPZs, and here we refer to these events as the critical AE event cluster. We, therefore, present and compare the characteristics of the critical AE event clusters of the representative tests for the three rock types (Fig. 8). The critical AE event clusters and the macrocrack photo of all the specimens are also provided in Figs. S2, S3 and S4 in the supplementary material. We also plot the density contours of the critical AE event clusters for the three rock types to better visualize the event distribution. The macrocracks on the front (red solid line in Fig. 8) and the back surface (red dotted line in Fig. 8) of the failed SCB specimens are traced and presented in the scatter and density contour plots.

1. SCB-G3 (Granite): The critical AE event cluster mainly concentrates near the notch tip and beside the macrocrack path. They distribute in an ellipse shape with the long and short axes of the ellipse parallel and perpendicular to the notch plane, respectively. The area with the largest event density is located ahead of the notch tip where the surface macrocracks traverse.
2. SCB-M2 (Marble): Similar to the granite, the critical AE event cluster mainly

concentrates near the notch tip and beside the macrocrack path. The shapes of the event density contours are generally elliptical. Both the front and back surface macrocracks traverse the largest event density area.

3. SCB-S5 (Sandstone): The critical AE event cluster distributes along the macrocrack paths, and only a few AE events are observed in the other area. The event density contours are a strip-like shape along the macrocrack path.

In summary, there are significant differences in the event number and distribution of the critical AE event clusters among the three rocks. The events in the granite and marble specimens mainly concentrate in front of the notch tip in the elliptical regions, but those in the sandstone scatter in a narrow strip along the macrocrack path. As shown in Fig. 6b and Fig. 8 much more AE events are detected in the granite as compared with the marble and sandstone. The mean maximum AE event density (D_m) of the granite, marble and sandstone are 13.3, 2.2 and 1.8 mm^{-2}, respectively. The D_m values of the five SCB granite specimens are the most scattered, while those of the five SCB sandstone specimens are the least scattered (Fig. 8d). In granite, there are substantial AE events behind the notch tip, in contrast, only a few AE events are observed behind the notch tip for the sandstone.

3.2.2 Source mechanisms and relative amplitudes of AE events

As mentioned in section 2.3, the AE events are classified into tensile, shear and collapse events based on their source mechanisms. Fig. 9 presents the percentages of tensile, shear and collapse events constituting the critical AE event clusters of all the tested specimens. The mean percentages of tensile events are 86 % and 78 % for the marble and sandstone, respectively,

which are significantly larger than that of the granite at 60%. The mean percentages of shear events of the granite, marble and sandstone are 33 %, 12 % and 20 %, respectively. For all three rock types, the collapse events account for less than 15 % of all the events. To summarize, the tensile events are the predominant event type for the three rock types. More shear events are observed in the granite as compared with the marble and sandstone.

To further compare the AE characteristics of the three rocks, we present the spatial distribution of the critical AE event clusters, with different amplitudes and source mechanisms in the typical SCB tests on the granite (Fig. 10), marble (Fig. 11) and sandstone (Fig. 12). Because the collapse events only account for a small proportion (less than 15 %) of the total events for the three rock types, we only focus on the distributions of tensile and shear events and plot their distributions separately.

1. SCB-G3 (Granite): The tensile and shear events have a similar spatial distribution pattern with most of the events concentrating around the notch tip (Fig. 10 b–c). The number of tensile AE events behind the notch tip is larger than that of shear AE events. Most high-amplitude events concentrate at the center of the cluster, and in contrast, low-and medium amplitude events distribute in a wider elliptical region (Fig. 10 d–f).
2. SCB-M2 (Marble): The tensile events account for most of the AE events. Only a few shear events scatter mainly around the notch tip (Fig. 11 a–c). Most of the high-amplitude events concentrate around the notch tip, and for the low- and medium-amplitude events, apart from those concentrating in the vicinity of the notch tips, we can also observe a number of AE events scattering beside the central notch plane far away from the notch tip (Fig. 11 d–f).

335 3. SCB-S5 (Sandstone): The tensile events mainly distribute ahead of the notch tip, and
336 most shear events are located at the upper portion of the specimen (Fig. 12 a–c). The
337 tensile AE events could possess different amplitudes, and most shear events have
338 medium or large amplitudes. The relative amount of low- and medium-amplitude AE
339 events is much smaller than in the granite and marble (Fig. 12 d–e). The high-
340 amplitude AE events are mainly distributed in two regions (Fig. 12f). One of the
341 regions is located at the notch tip and another one is at the far end of the macrocracks
342 path near the specimen boundary.

343 ## 3.3 Thin-section petrographic analysis results

344 The microscopic view besides the macrocracks induced in the SCB tests with vertical
345 distance 10 mm from the notch tips (Fig. 13a) of the three rock types are examined and
346 characterized:

347 1. Granite (Fig. 13b): The macrocrack in the granite consists of a number of segments
348 of intergranular and transgranular cracks. The intergranular crack is defined as the
349 crack formed along the boundaries of two adjacent mineral grains. The transgranular
350 crack is defined as the crack that grows through the mineral grains. The method to
351 identify these two cracks via thin-section petrographic analysis is detailed in Wong
352 et al., (2019). There are large numbers of microcracks in the mineral grains beside
353 the macrocrack. More microcracks are observed in the quartz than other mineral
354 grains. The microcrack widths are less than 0.1 mm. Their lengths are around 1-2
355 mm. Most of the microcracks are subparallel to the macrocrack (See Fig. S5 in the

supplementary material).

2. Marble (Fig. 13c): Similar to the granite, both intergranular and transgranular cracks constitute the macrocrack. Microcracks are occasionally observed in the dolomite grains beside the macrocrack. The lengths of these microcracks have a similar order of amplitude of the grain size (0.3-0.4 mm). The number and length of the microcracks in the marble are much smaller than those in the granite.
3. Sandstone (Fig. 13d): The macrocrack in sandstone generally propagate through the cement materials and along the grain boundaries (intergranular cracks). There are very few microcracks in the mineral grains beside the macrocrack.

4 Discussion

4.1 The relation between AE events and pre-existing microcracks

Stress concentration occurs ahead of the notch tip of the SCB specimen under loading. When the local stress exceeds the local strength, new microcracks could initiate and pre-existing microcracks could open/shear/propagate accompanied by the radiation of elastic waves (i.e. AEs). In this study, we conduct the SCB tests on the granite, marble and sandstone specimens and monitor the AEs simultaneously. Because we mainly focus on the AEs induced by the development of FPZ, only the characteristics of AE events detected before the initiation of macrocracks are analyzed and compared. The spatial-temporal evolution and source mechanisms of AE events detected before the initiation of macrocracks are analyzed and compared. However, one should keep in mind that a recorded signal may not be the equivalent of an AE event. Owing to the geometry of the SCB sample, AE waveforms may be reflected and diffracted, creating false triggered events. Due to the attenuation during the reflection and diffraction, the amplitude of the false triggered events will be smaller than the true AE events. Therefore, it could be more important to pay attention to the AE events with relatively large energy. We observed a number of AE events below the notch tips, especially for granite and marble. This could be counterintuitive because the microcracks should mainly develop ahead of the notch tip where the local stress exceeds the strength as predicted by the Schmidt model (Schmidt, 1980). Most of these AE events have small and moderate amplitudes, which suggest that they may be induced by factors such as the reflection and diffraction of elastic waves induced by the pre-existing notch, movements of pre-existing microcracks adjacent to the notch

386 tip, and location error due to weak signals.

387 We observed the most AE events in the granite and the least in the sandstone. Based on
388 the thin-section petrographic analysis results of the untested samples (Fig. 1), the most and
389 longest pre-existing microcracks are spotted in the granite. Relatively fewer microcracks are
390 observed in the marble and the least microcracks in the sandstone. It is evident that the
391 differences in the AE characteristics of the three rocks in the SCB tests are closely associated
392 with their distinct pre-existing microcrack features. Pre-existing microcracks could serve as
393 planes of weakness and be reactivated under loading and emit AEs. Thus, the more pre-existing
394 microcracks, the more AEs during the failure process. This observation is consistent with the
395 finding in our previous study on granite (Guo et al., 2021).

396 The spatial distribution pattern of AE events in granite and marble samples (i.e. two
397 fissured crystalline rocks) is different from that in the sandstone. The AE events in the granite
398 and marble both concentrate around the notch tip, while those in the sandstone distribute along
399 the macrocrack path. The AE events distributed around the notch tip of granite and marble may
400 be related to the pre-existing microcracks, as they are more likely to be mobilized under the
401 stress concentration. The higher number of pre-existing microcracks in granite resulted in a
402 larger total number of AE and a larger region with AE activities compared to the marble. In
403 contrast, the sandstone is a porous nonfissured rock and its microstructure is different from the
404 two crystalline rocks. The mineral grains of the sandstone are held together by the cement with
405 very few pre-existing microcracks. The macrocrack in the sandstone mainly propagates
406 through the cement materials and along the grain boundaries. Because there are few
407 microcracks in the mineral grains, the AEs in the sandstone could be mostly induced by the

nucleation and propagation of new microcracks in the areas where the macrocrack would subsequently form.

The temporal distribution of the AE events in three types of rock specimens is similar: the number of the AE events increases slowly during loading followed by an exponential increase before the failure. The exponential increase of the AE events has been identified as a precursor of the catastrophic failure of rocks under compressive loading (e.g. Diederichs et al., 2004; Zhao et al., 2015; He et al., 2018). In this study, we observe this phenomenon in a tensile loading scheme (i.e. the SCB test), and the exponential increase of the AE indicates unstable fracturing that involves interaction and coalescence of microcracks.

The analysis of the source mechanisms of the AE events of the three rocks shows that for all the three rock types, the tensile events are the predominant event type which is consistent with the tensile nature of this mode I loading test. Much more shear events are observed in the granite as compared with the marble and sandstone. The formation mechanism of shear events may be related to the grain-scale defects such as pre-existing microcracks, cleavages and mineral boundaries. The loading scheme of the SCB test introduces maximum tensile stress normal to the pre-existing notch. The initiation and propagation of these defects whose planes are oblique to the tensile stress could result in the shear events. Therefore, more shear events are observed in the granite with more pre-existing microcracks as compared with the marble and sandstone.

4.2 Implication to the interpretation of laboratory and field seismic activities

Although large numbers of studies have investigated the microcracking behaviour or

429 micro-damage of different rocks using the AE technique, few have made direct comparisons
430 among the AE results on different rock types (Li & Einstein, 2020). The AE results may be
431 largely influenced by many factors such as rock type, loading condition, experimental setup
432 and AE data analysis protocol. Direct comparison of AE characteristics of different rocks
433 among different laboratories under different testing setups could be misleading. Our study
434 provides a benchmark that excludes the influencing factors except for rock type. Our results
435 shed light on interpreting AE results in laboratory fracturing tests on different rocks. For
436 example, in terms of the spatial distribution of AE events, this study elucidates that the AE
437 events in the fissured crystalline rocks (e.g. granite and marble) concentrate ahead of the notch
438 tip in elliptical regions, while those in the nonfissured sandstone distribute generally along the
439 macrocrack path. Therefore, it would be more feasible to predict the macrocrack pathway from
440 the distribution of the AE events detected before the initiation of macrocrack in sandstone than
441 granite and marble.

442 Apart from the laboratory-scale seismicity (AE), this research also provides useful
443 insights into interpreting or understanding the seismic activities at the scale of geotechnical
444 engineering, namely microseismicity. Microseismicity monitoring has been applied to detect
445 and mitigate the geo-disasters related to the catastrophic initiation and propagation of cracks at
446 different scales such as slope instability (Ma et al., 2017) and rockburst (Ma et al., 2020). The
447 number and energy of micro-seismic events are always used for warning of rockburst (Feng,
448 2017). The results of our laboratory test show that before the initiation of macrocracks, the
449 parameters such as maximum AE event rate and cumulative AE event number vary with the
450 rock type. It may be unreasonable to adopt the constant micro-seismic event-related parameters

for conceiving the criteria for warning and predicting the geo-disasters in geotechnical engineering with different host rocks. Through characterization of the microscopic characteristics of the rock is suggested to be conducted to have a better understanding of the seismic characteristics of the host rocks during fracturing.

4.3 AE technique limitations and biases of the AE results

Although the AE technique is robust in monitoring microcracking, there are still limitations. In laboratory rock fracture or deformation tests, the frequency of AEs generally ranges from 100 kHz to 2000 kHz (Lockner 1993). The operating frequency of the sensors used in this study is from 200 to 750 kHz, which means the sensors would be less sensitive to the relatively low-frequency (<200 kHz) and high-frequency (>750kHz) AEs. Consequently, some bias will be introduced in the AE results by the relatively narrow frequency band of the sensors. The AE event localization and source mechanism results could be less biased by the narrow frequency band because we use only the P wave arrival for AE event localization and the polarities of the first peaks of P waves for determining source mechanisms. However, the signal energy and the relative amplitude of the low-frequency and high-frequency AEs may be underestimated compared to those with medium frequency (200-750 kHz).

5. Conclusions

In this study, we conduct a comparative experimental study of AE characteristics during the microcracking processes of the granite, marble and sandstone under mode I loading. We compare the number, rate, spatial-temporal evolution, amplitudes and source mechanisms of AE events of three rocks. Combined with the thin-section petrographic analysis, we discuss the mechanisms of different AE characteristics from the microscopic perspective. We find that the temporal evolution patterns of AE events are generally similar among the three rock types. The AE event number first increases linearly, then exponentially as the sample approaches failure. The spatial distributions of the AE events are highly correlated to the microscopic features of the rocks. The AE events in the two fissured crystalline rocks, namely granite and marble, concentrated near the notch tip; while the AE events in the nonfissured sandstone distribute generally along the macrocrack path. The total number of AE events is closely related to the number of the pre-existing microcracks in the rock, with the most AE events observed in the strongly fissured granite and least in the nonfissured sandstone. In terms of source mechanisms of AE events, the tensile events are the predominant event type for all the tests. Much more shear events are observed in the granite as compared with the marble and sandstone. The differences in the quantity and source mechanisms of AE events are closely related to the distinct microcracking mechanisms of the three rocks. These results improve the understanding of the relation between microscopic cracking behaviour and AEs for different rocks and suggest that AE analysis should be conducted with microscopic characteristics taken into account, as the event number, location, and mechanism of the AE events may be drastically different for

different rock types.

Acknowledgment

The authors would like to thank the editor, Dr Bing Li, and the anonymous reviewer for their valuable suggestions. The authors acknowledge the support from the FCE Start-up Fund for New Recruits at the Hong Kong Polytechnic University (P0034042), the Early Career Scheme of the Research Grants Council of the Hong Kong Special Administrative Region, China (Project No. PolyU 25220021), and the Distinguished Postdoctoral Fellowship Scheme at the Hong Kong Polytechnic University (P0039280).

Statements and Declarations

Conflict of interest The authors declare that there is no conflict of interest.

References

Akaike, H. (1998). Information theory and an extension of the maximum likelihood principle. In Selected papers of hirotugu akaike (pp. 199-213). Springer, New York, NY.

ASTM D1316-21. (2021). Standard Terminology for Nondestructive Examinations, ASTM International, West Conshohocken, PA.

Ashby, M. F., and S. D. Hallam (1986), The failure of brittle solids containing small cracks under compressive stress states, Acta Metall., 34(3), 497–510.

Backers, T., Stanchits, S., & Dresen, G. (2005). Tensile fracture propagation and acoustic emission activity in sandstone: The effect of loading rate. International journal of rock mechanics and mining sciences, 42(7-8), 1094-1101.

Barenblatt, G. I. (1959). The formation of equilibrium cracks during brittle fracture. General ideas and hypotheses. Axially-symmetric cracks. Journal of Applied Mathematics and Mechanics, 23(3), 622-636.

Bunger, A. P., Kear, J., Dyskin, A. V., & Pasternak, E. (2015). Sustained acoustic emissions following tensile crack propagation in a crystalline rock. International Journal of Fracture, 193(1), 87-98.

Carpinteri, A., Xu, J., Lacidogna, G., & Manuello, A. (2012). Reliable onset time determination and source location of acoustic emissions in concrete structures. Cement and concrete composites, 34(4), 529-537.

Chandler, M. R., Fauchille, A. L., Kim, H. K., Ma, L., Mecklenburgh, J., Rizzo, R., Mostafavi, M., Marussi, S., Robert, A., May, S., Azeem, M., Rutter, E., Taylor, K., Lee P. (2018). Correlative optical and X-ray imaging of strain evolution during double-torsion fracture toughness measurements in shale. Journal of Geophysical Research: Solid Earth, 123(12), 10-517.

Chang, S. H., Lee, C. I., & Jeon, S. (2002). Measurement of rock fracture toughness under modes I and II and mixed-mode conditions by using disc-type specimens. Engineering geology, 66(1-2), 79-97.

Chen, Y., Xu, J., Peng, S., Jiao, F., Chen, C., & Xiao, Z. (2021). Experimental study on the acoustic emission and fracture propagation characteristics of sandstone with variable angle joints. Engineering Geology, 106247.

Diederichs, M. S., Kaiser, P. K., & Eberhardt, E. (2004). Damage initiation and propagation in hard rock during tunnelling and the influence of near-face stress rotation. International Journal of Rock Mechanics and Mining Sciences, 41(5), 785-812.

Dugdale, D. S. (1960). Yielding of steel sheets containing slits. Journal of the Mechanics and Physics of Solids, 8(2), 100-104.

Feng, X. T. (2017). Rockburst: mechanisms, monitoring, warning, and mitigation. Butterworth-Heinemann.

Friedman, M., Handin, J., & Alani, G. (1972). Fracture-surface energy of rocks. International Journal of Rock Mechanics and Mining Sciences & Geomechanics Abstracts, 9 (6), 757-764.

Funatsu, T., Shimizu, N., Kuruppu, M., & Matsui, K. (2015). Evaluation of mode I fracture

toughness assisted by the numerical determination of K-resistance. Rock Mechanics and Rock Engineering, 48(1), 143-157

Geiger, L. (1910). Herdbestimmung bei Erdbeben aus den Ankunftszeiten, Nachrichten der K. Gesellschaft der Wissenschaften zu Gottingen. Math.-Phys. Klasse, 331-349.

Geiger, L. (1912). Probability method for the determination of earthquake epicentres from the arrival time only, Bull. St. Louis. Univ. 8, 60-71.

Graham, C. C., Stanchits, S., Main, I. G., & Dresen, G. (2010). Comparison of polarity and moment tensor inversion methods for source analysis of acoustic emission data. International journal of rock mechanics and mining sciences, 47(1), 161.

Guo, T. Y., & Wong, L. N. Y. (2020). Microcracking behavior of three granites under mode I loading: Insights from acoustic emission. Engineering Geology, 278, 105823.

Guo, T. Y., & Wong, L. N. Y. (2021). Cracking mechanisms of a medium-grained granite under mixed-mode I-II loading illuminated by acoustic emission. International Journal of Rock Mechanics and Mining Sciences, 145, 104852.

Guo, T. Y., Wong, L. N. Y., & Wu, Z. (2021). Microcracking behavior transition in thermally treated granite under mode I loading. Engineering Geology, 282, 105992.

He, T. M., Zhao, Q., Ha, J., Xia, K., & Grasselli, G. (2018). Understanding progressive rock failure and associated seismicity using ultrasonic tomography and numerical simulation. Tunnelling and Underground Space Technology, 81, 26-34.

Hoagland, R. G., Hahn, G. T., & Rosenfield, A. R. (1973). Influence of microstructure on fracture propagation in rock. Rock mechanics, 5(2), 77-106.

Huang R.Q. (2007). Large-scale landslides and their sliding mechanisms in China since the 20th century. Chinese Journal of Rock Mechanics and Engineering, 26(3), 433-454.

Irwin, G. (1997). Plastic zone near a crack and fracture toughness.

Kao, C. S., Carvalho, F., & Labuz, J. (2011). Micromechanisms of fracture from acoustic emission. International Journal of Rock Mechanics and Mining Sciences, 48(4), 666-673.

Kataoka, M., Obara, Y., & Kuruppu, M. (2015). Estimation of fracture toughness of anisotropic rocks by semi-circular bend (SCB) tests under water vapor pressure. Rock Mechanics and Rock Engineering, 48(4), 1353-1367.

Kong, R., Tuncay, E., Ulusay, R., Zhang, X., & Feng, X. T. (2021). An experimental investigation on stress-induced cracking mechanisms of a volcanic rock. Engineering Geology, 280, 105934.

Kuruppu, M. D., Obara, Y., Ayatollahi, M. R., Chong, K. P., & Funatsu, T. (2014). ISRM-suggested method for determining the mode I static fracture toughness using semi-circular bend specimen. Rock Mechanics and Rock Engineering, 47(1), 267-274.

Kwiatek, G., Goebel, T. H. W., & Dresen, G. (2014). Seismic moment tensor and b value variations over successive seismic cycles in laboratory stick-slip experiments. Geophysical Research Letters, 41(16), 5838-5846.

Labuz, J., Shah, S., & Dowding, C. (1985). Experimental analysis of crack propagation in granite. International Journal of Rock Mechanics and Mining Sciences & Geomechanics Abstracts.

Labuz, J., Shah, S., & Dowding, C. (1987). The fracture process zone in granite: evidence and effect. the International Journal of Rock Mechanics and Mining Sciences & Geomechanics

583 Abstracts.
584 Labuz, J. F., & Biolzi, L. (1998). Characteristic strength of quasi-brittle materials. International
585 Journal of Solids and Structures, 35(31-32), 4191-4203.
586 Lee, H. P., Olson, J. E., Holder, J., Gale, J. F., & Myers, R. D. (2015). The interaction of
587 propagating opening mode fractures with preexisting discontinuities in shale. Journal of
588 Geophysical Research: Solid Earth, 120(1), 169-181.
589 Li, B. Q., Moradian, Z., Goncalves da Silva, B., & Germaine, J. T. (2015). Observations of
590 acoustic emissions in a hydraulically loaded granite specimen. 49th US Rock
591 Mechanics/Geomechanics Symposium.
592 Li, B. Q., & Einstein, H. H. (2017). Comparison of visual and acoustic emission observations
593 in a four point bending experiment on barre granite. Rock Mechanics and Rock
594 Engineering, 50(9), 2277-2296.
595 Li, B. Q., & Einstein, H. H. (2019). Direct and microseismic observations of hydraulic
596 fracturing in barre granite and opalinus clayshale. Journal of Geophysical Research: Solid
597 Earth, 124(11), 11900-11916.
598 Li, B. Q., & Einstein, H. H. (2020). Normalized radiated seismic energy from laboratory
599 fracture experiments on Opalinus Clayshale and Barre Granite. Journal of Geophysical
600 Research: Solid Earth, 125(3), e2019JB018544.
601 Li, B. Q., da Silva, B. G., & Einstein, H. (2019). Laboratory hydraulic fracturing of granite:
602 acoustic emission observations and interpretation. Engineering Fracture Mechanics, 209,
603 200-220.
604 Li, X., Lei, X., & Li, Q. (2021). Fault nucleation of tight sandstone by investigation of
605 mechanical, acoustic, and hydraulic responses. Engineering Geology, 106254.
606 Lin, Q., Wan, B., Wang, Y., Lu, Y., & Labuz, J. F. (2019). Unifying acoustic emission and digital
607 imaging observations of quasi-brittle fracture. Theoretical and Applied Fracture
608 Mechanics, 103, 102301.
609 Lin, Q., Wang, S., Wan, B., Lu, Y., & Wang, Y. (2020). Characterization of Fracture Process in
610 Sandstone: A Linear Correspondence Between Acoustic Emission Energy Density and
611 Opening Displacement Gradient. Rock Mechanics and Rock Engineering, 53(2), 975-981.
612 Lockner, D., Byerlee, J. D., Kuksenko, V., Ponomarev, A., & Sidorin, A. (1991). Quasi-static
613 fault growth and shear fracture energy in granite. Nature, 350(6313), 39-42.
614 Lockner, D. (1993). The role of acoustic emission in the study of rock fracture. Paper presented
615 at the International Journal of Rock Mechanics and Mining Sciences & Geomechanics
616 Abstracts.
617 Ma, C., Li, T., & Zhang, H. (2020). Microseismic and precursor analysis of high-stress hazards
618 in tunnels: A case comparison of rockburst and fall of ground. Engineering Geology, 265,
619 105435.
620 Ma, K., Tang, C. A., Liang, Z. Z., Zhuang, D. Y., & Zhang, Q. B. (2017). Stability analysis and
621 reinforcement evaluation of high-steep rock slope by microseismic monitoring.
622 Engineering Geology, 218, 22-38.
623 Mahanta, B., Singh, T. N., & Ranjith, P. G. (2016). Influence of thermal treatment on mode I
624 fracture toughness of certain Indian rocks. Engineering Geology, 210, 103-114.
625 Meng, F., Wong, L. N. Y., Zhou, H., & Wang, Z. (2018). Comparative study on dynamic shear

behavior and failure mechanism of two types of granite joint. Engineering Geology, 245, 356-369.

Meng, F., Wong, L. N. Y., Zhou, H., Wang, Z., & Zhang, L. (2020). Asperity degradation characteristics of soft rock-like fractures under shearing based on acoustic emission monitoring. Engineering Geology, 266, 105392.

Meng, F., Wong, L. N. Y., Zhou, H., Yu, J., & Cheng, G. (2019). Shear rate effects on the post-peak shear behaviour and acoustic emission characteristics of artificially split granite joints. Rock Mechanics and Rock Engineering, 52(7), 2155-2174.

Nasseri, M., Mohanty, B., & Young, R. (2006). Fracture toughness measurements and acoustic emission activity in brittle rocks. Pure and Applied Geophysics, 163(5-6), 917-945.

Ohtsu, M. (1991). Simplified moment tensor analysis and unified decomposition of acoustic emission source: application to in situ hydrofracturing test. Journal of Geophysical Research: Solid Earth, 96(B4), 6211-6221.

Ohtsu, M. (1995). Acoustic emission theory for moment tensor analysis. Research in Nondestructive Evaluation, 6(3), 169-184.

Olasolo, P., Juárez, M. C., Morales, M. P., & Liarte, I. A. (2016). Enhanced geothermal systems (EGS): A review. Renewable and Sustainable Energy Reviews, 56, 133-144.

Parisio, F., Tarokh, A., Makhnenko, R., Naumov, D., Miao, X. Y., Kolditz, O., & Nagel, T. (2019). Experimental characterization and numerical modelling of fracture processes in granite. International Journal of Solids and Structures, 163, 102-116.

Schmidt, R. A. (1980) A microcrack model and its significance to hydraulic fracturing and fracture toughness testing. In: Presented at the 21st US symposium on rock mechanics (USRMS), Rolla, Missouri

Tal, Y., Evans, B., & Mok, U. (2016). Direct observations of damage during unconfined brittle failure of Carrara marble. Journal of Geophysical Research: Solid Earth, 121(3), 1584-1609.

Tarokh, A., Makhnenko, R. Y., Fakhimi, A., & Labuz, J. F. (2017). Scaling of the fracture process zone in rock. International Journal of Fracture, 204(2), 191-204.

Tester, J. W., Anderson, B. J., Batchelor, A. S., Blackwell, D. D., DiPippo, R., Drake, E. M., ... & Veatch, R. J. (2006). The future of geothermal energy. Massachusetts Institute of Technology, 358.

Tutluoglu, L., & Keles, C. (2011). Mode I fracture toughness determination with straight notched disk bending method. International Journal of Rock Mechanics and Mining Sciences, 48(8), 1248-1261.

Ulusay, R., & Hudson, J. A. (2007). The complete ISRM suggested methods for rock characterization, testing and monitoring: 1974-2006.

Wang, X., Wang, E., Liu, X., & Zhou, X. (2021). Failure mechanism of fractured rock and associated acoustic behaviors under different loading rates. Engineering Fracture Mechanics, 247, 107674.

Wang, S., Xu, W., Yan, L., Feng, X. T., Xie, W. C., & Chen, H. (2020). Experimental investigation and failure mechanism analysis for dacite under true triaxial unloading conditions. Engineering Geology, 264, 105407.

Wei, M. D., Dai, F., Xu, N. W., Zhao, T., & Xia, K. W. (2016a). Experimental and numerical

study on the fracture process zone and fracture toughness determination for ISRM-suggested semi-circular bend rock specimen. Engineering Fracture Mechanics, 154, 43-56.

Wei, M. D., Dai, F., Xu, N. W., Liu, J. F., & Xu, Y. (2016b). Experimental and numerical study on the cracked chevron notched semi-circular bend method for characterizing the mode I fracture toughness of rocks. Rock Mechanics and Rock Engineering, 49(5), 1595-1609.

Wei, M. D., Dai, F., Xu, N. W., Zhao, T., & Liu, Y. (2017). An experimental and theoretical assessment of semi-circular bend specimens with chevron and straight-through notches for mode I fracture toughness testing of rocks. International Journal of Rock Mechanics and Mining Sciences, 99, 28-38.

Wei, M., Dai, F., Liu, Y., Li, A., & Yan, Z. (2021). Influences of Loading Method and Notch Type on Rock Fracture Toughness Measurements: From the Perspectives of T-Stress and Fracture Process Zone. Rock Mechanics and Rock Engineering, 1-22.

Whittaker, B. N., Singh, R. N., & Sun, G. (1992). Rock fracture mechanics. Principles, design and applications.

Wong, L. N. Y., & Guo, T. Y. (2019). Microcracking behavior of two semi-circular bend specimens in mode I fracture toughness test. Engineering Fracture Mechanics, 106565.

Wong, L. N. Y., Guo, T. Y., Lam, W. K., & Ng, J. Y. H. (2019). Experimental study of cracking characteristics of Kowloon granite based on three mode I fracture toughness methods. Rock Mechanics and Rock Engineering, 52(11), 4217-4235.

Wong, L. N. Y., Guo, T. Y., Wu, Z., & Xiao, X. (2021). How do thermally induced microcracks alter microcracking mechanisms in Hong Kong granite? Engineering Geology, 106268.

Xu, N. W., Tang, C. A., Li, L. C., Zhou, Z., Sha, C., Liang, Z. Z., & Yang, J. Y. (2011). Microseismic monitoring and stability analysis of the left bank slope in Jinping first stage hydropower station in southwestern China. International Journal of Rock Mechanics and Mining Sciences, 48(6), 950-963.

Yao, Q., Tang, C., Xia, Z., Liu, X., Zhu, L., Chong, Z., & Hui, X. (2020). Mechanisms of failure in coal samples from underground water reservoir. Engineering Geology, 267, 105494.

Zang, A., Christian Wagner, F., Stanchits, S., Dresen, G., Andresen, R., & Haidekker, M. A. (1998). Source analysis of acoustic emissions in Aue granite cores under symmetric and asymmetric compressive loads. Geophysical Journal International, 135(3), 1113-1130.

Zhao, Q., & Glaser, S. D. (2020). Relocating acoustic emission in rocks with unknown velocity structure with machine learning. Rock Mechanics and Rock Engineering, 53(5), 2053-2061.

Zhao, Q., Tisato, N., Grasselli, G., Mahabadi, O. K., Lisjak, A., & Liu, Q. (2015). Influence of in situ stress variations on acoustic emissions: a numerical study. Geophysical Journal International, 203(2), 1246-1252.

Zhang, H., Fu, D., Song, H., Kang, Y., Huang, G., Qi, G., & Li, J. (2015). Damage and fracture investigation of three-point bending notched sandstone beams by DIC and AE techniques. Rock Mechanics and Rock Engineering, 48(3), 1297-1303.

Zhang, Z., Li, Y., Hu, L., & Zheng, H. (2021). Predicting rock failure with the critical slowing down theory. Engineering Geology, 280, 105960.

Zheng, Z., Feng, X. T., Yang, C. X., Zhang, X. W., Li, S. J., & Qiu, S. L. (2020). Post-peak deformation and failure behaviour of Jinping marble under true triaxial stresses.

712 **Table 1** Summary of experimental studies of the AE characteristics during the microcracking processes
713 of different rocks under static mode I loading

Authors	Rock types	AE characteristics	Mode I loading configurations
Hoagland et al. (1973)	Limestone, Sandstone	AE count	Double-cantilever-beam (DCB) specimen under wedge loading
Labuz et al. (1987)	Granite	AE location	DCB specimen under wedge loading
Labuz & Biolzi (1998)	Granite; Sandstone	AE location	Pre-notched and smooth beam specimen under four-point bending
Backers et al. (2005)	Sandstone	AE location, AE source mechanisms	Chevron bend specimen under three-point bending
Nasseri et al. (2006)	Granite	AE location, Ae source mechanisms	Chevron cracked notch Brazilian disc (CCNBD) specimen
Kao et al. (2011)	Granite	AE location, AE source mechanisms	Pre-notched beam under three-point bending
Bunger et al., (2015)	Gabbro	AE location, AE event energy	Pre-notched beam under three-point bending
Zhang et al., (2015)	Sandstone	AE count	Pre-notched beam under three-point bending
Wei et al. (2016a)	Sandstone	AE location	Semi-circular bend (SCB) specimen under three-point bending
Li & Einstein (2017)	Granite	AE location, AE event energy, AE source mechanisms	Pre-notched beam under four-point bending
Tarokh et al. (2017)	Granite	AE location	Pre-notched beam under three-point bending
Li & Einstein (2019)	Granite; Shale	AE amplitude, AE hit, AE location, AE source mechanisms	Pre-cut prismatic specimen subjected to hydraulic fracturing
Lin et al. (2019)	Sandstone	AE location, AE event energy	Pre-notched beam specimen under three-point bending
Parisio et al. (2019)	Granite	AE location	Pre-notched beam specimen under three-point bending
Wong & Guo (2019)	Granite	AE location, AE event energy	SCB specimen under three-point bending
Lin et al. (2020)	Sandstone	AE location, AE event energy	Pre-notched beam specimen under three-point bending
Guo & Wong (2020)	Granite	AE location	SCB specimen under three-point bending
Guo et al. (2021)	Granite	AE location	SCB specimen under three-point bending
Wong et al. (2021)	Granite	AE event energy AE source mechanisms	SCB specimen under three-point bending
Guo & Wong (2021)	Granite	AE location AE source mechanisms	SCB specimen under three-point bending

714

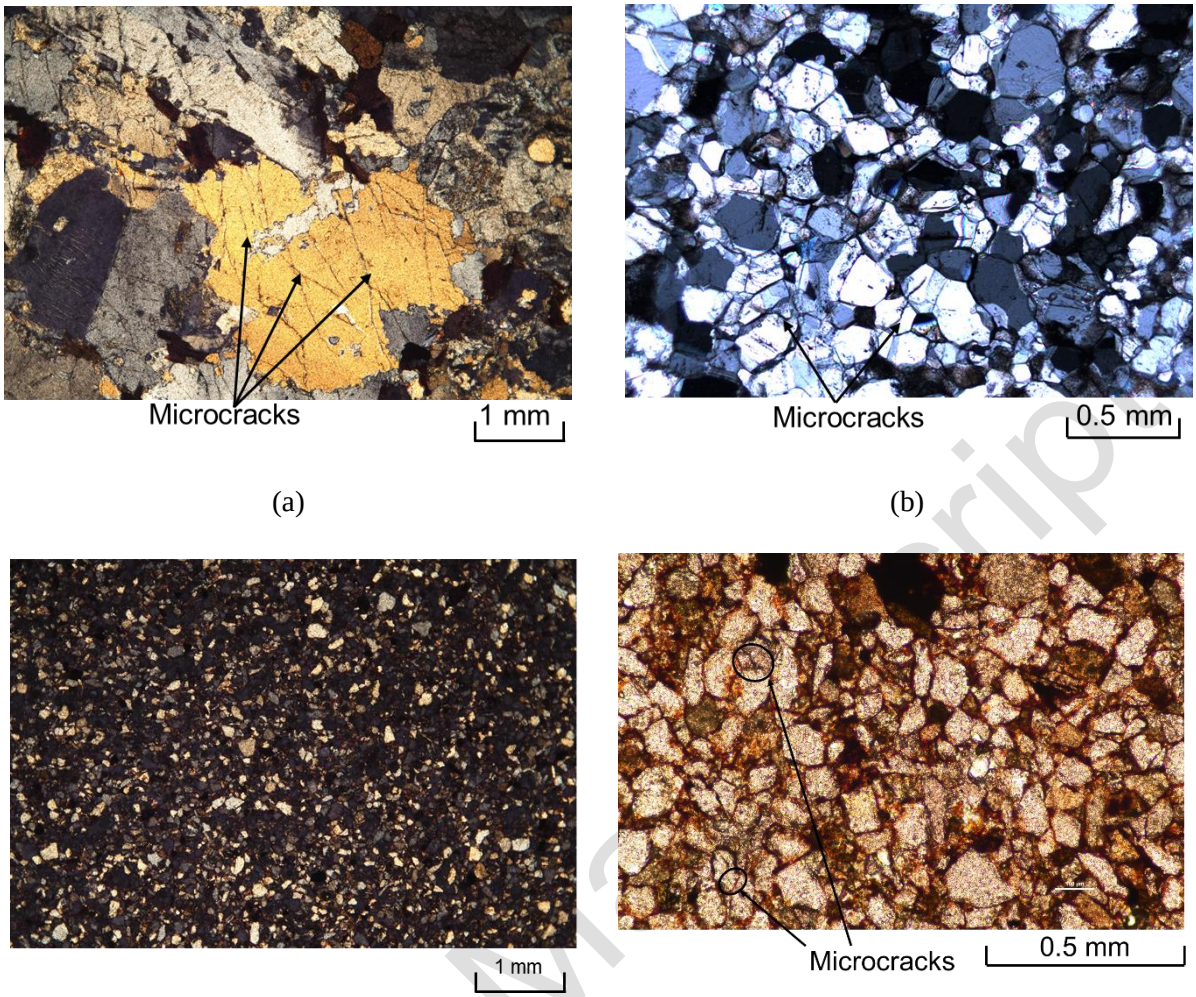

(a) (b)

(c) (d)

Fig. 1 Thin-section photos of (a) granite, (b) marble and (c) sandstone under cross-polarized light (XPL). (d) A zoom-in view of the sandstone under plane-polarized light (PPL)

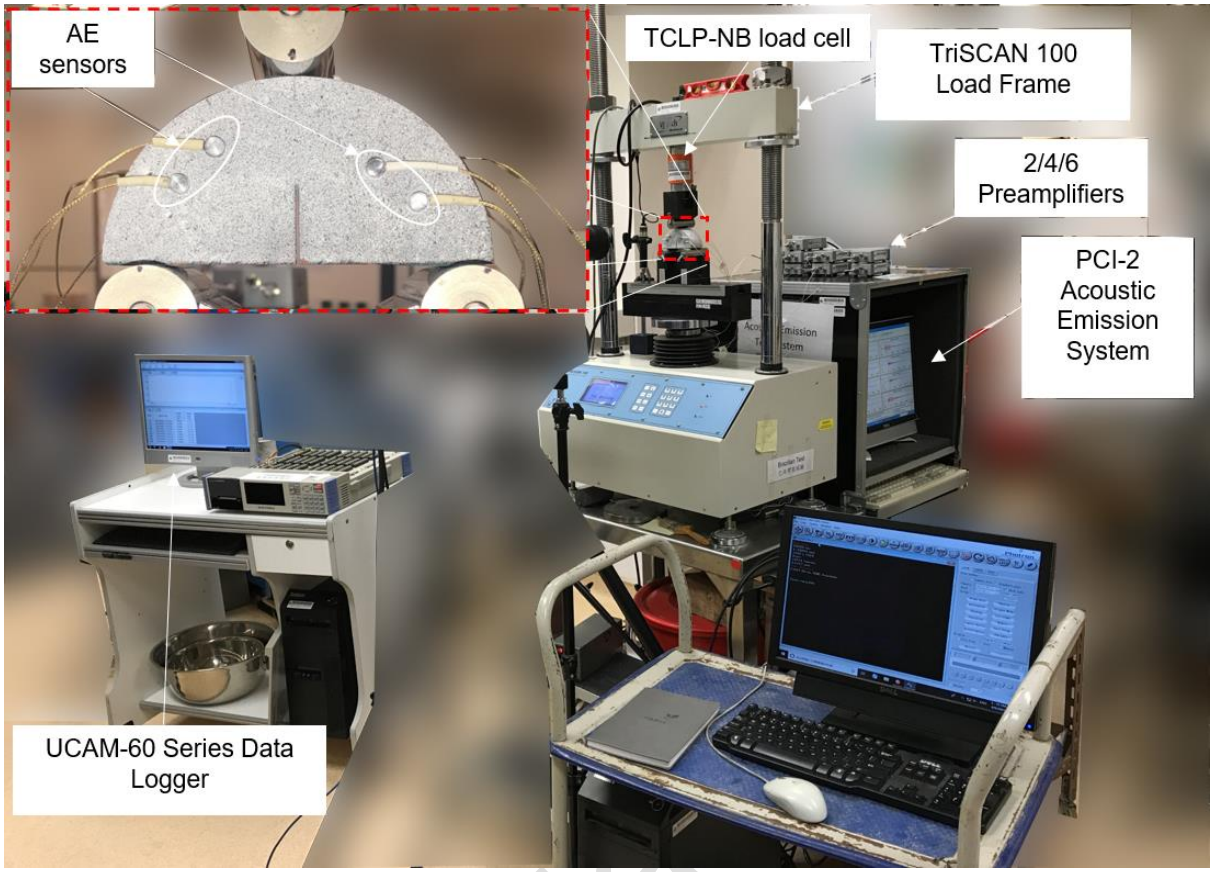
AE sensors
TCLP-NB load cell
TriSCAN 100 Load Frame
2/4/6 Preamplifiers
PCI-2 Acoustic Emission System
UCAM-60 Series Data Logger

(a)

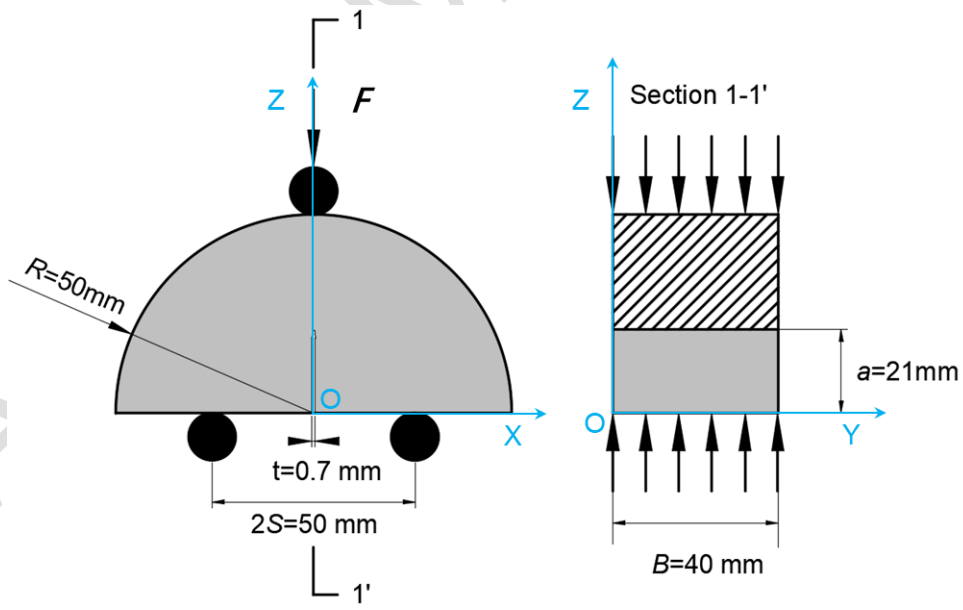
1
Z
F
R=50mm
O
X
t=0.7 mm
2S=50 mm
1'
Z
Section 1-1'
a=21mm
O
Y
B=40 mm

(b)

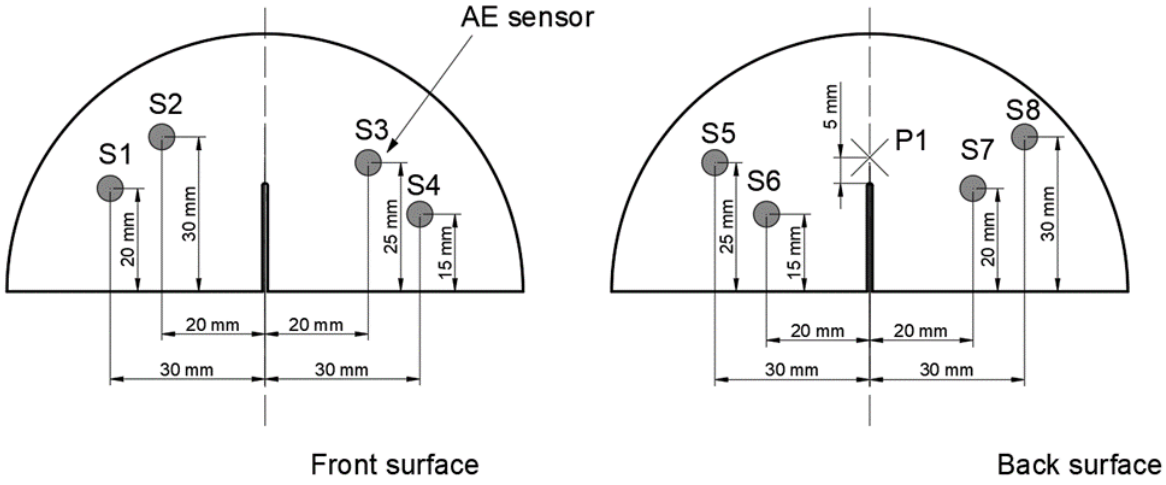

(c)

Fig. 2 (a) Experimental setup of the semi-circular bending (SCB) test and acoustic emission (AE) test. (b) Specimen geometry and loading scheme of the SCB tests. *R* and *B* denote the radius and thickness of the SCB specimen, respectively. *F* indicates the axial load. *t* and *a* are the width and length of the straight-through notch. The black circles on the top and bottom of the specimen are the loading and supporting rollers of the three-point bending fixture. *S* is the half span of the supporting roller. The coordinate system is presented for the convenience of AE event localization. (c) The locations of the AE sensor (S1-S8) on the front and back surfaces of the SCB specimen. P1 (marked with the cross) denotes the location of the pencil lead break test (Colorful online)

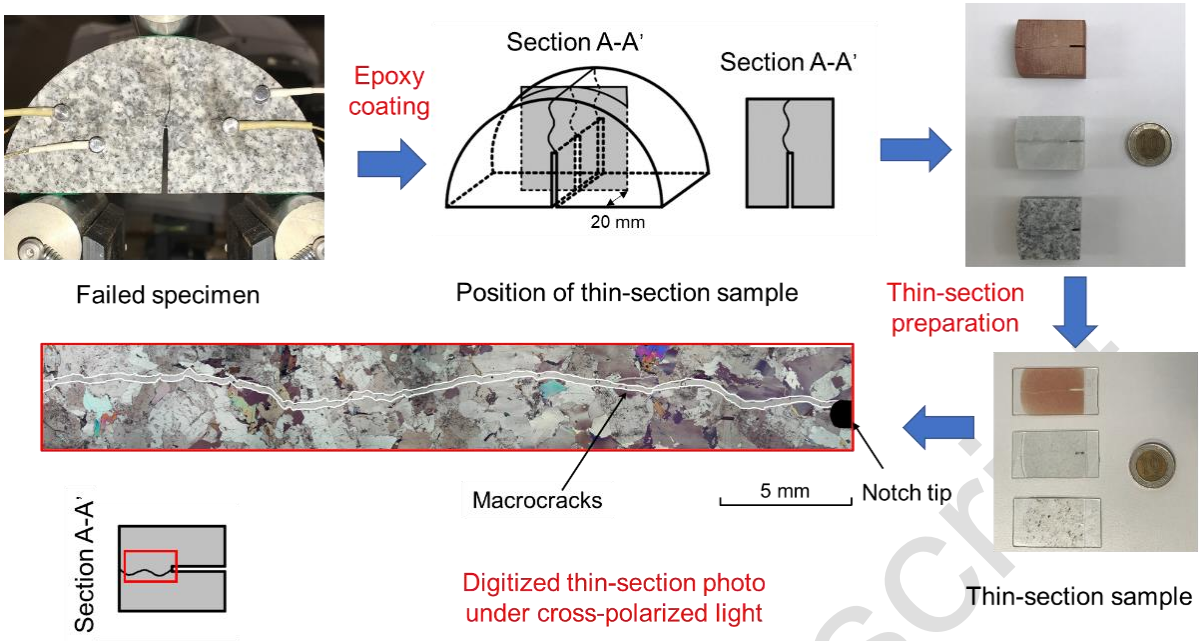

735

736 **Fig. 3** Preparation procedures of the thin-section samples containing the macrocracks induced in the
737 SCB tests (Colorful online)

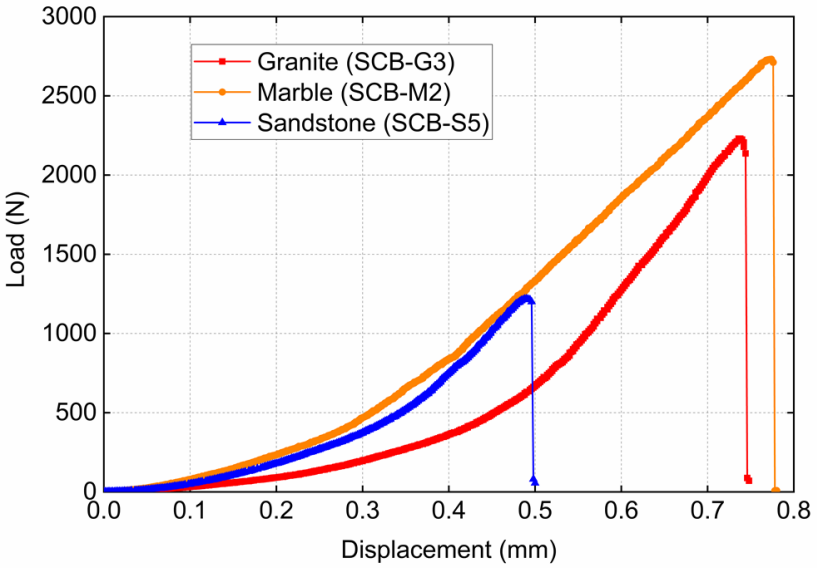

738

739 (a)

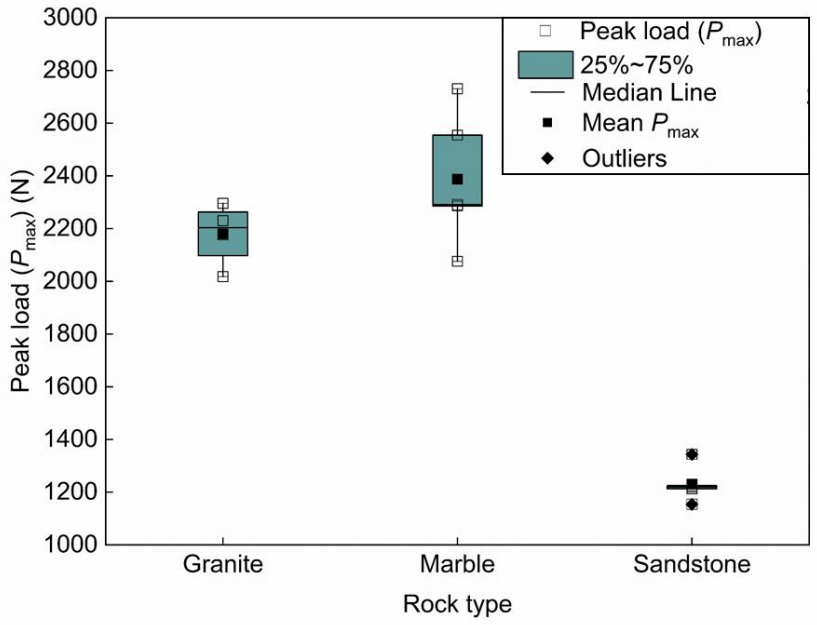

740

741 (b)

742

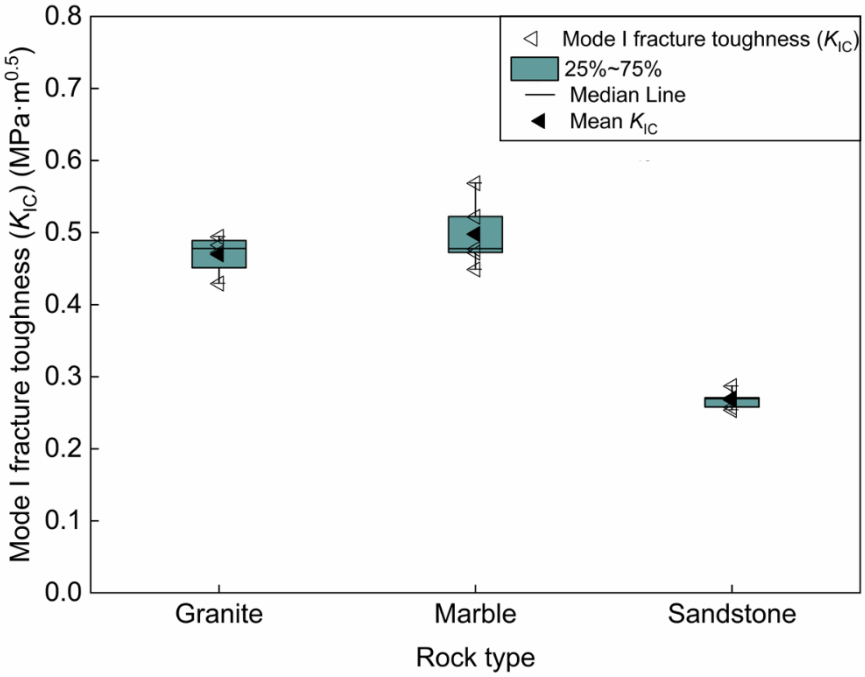

(c)

Fig. 4 (a) Typical axial load versus displacement curves of the granite, marble and sandstone specimens in the SCB tests. Summary of the (b) peak load of all the granite, marble and sandstone specimens in the SCB tests and (c) measured mode I fracture toughness

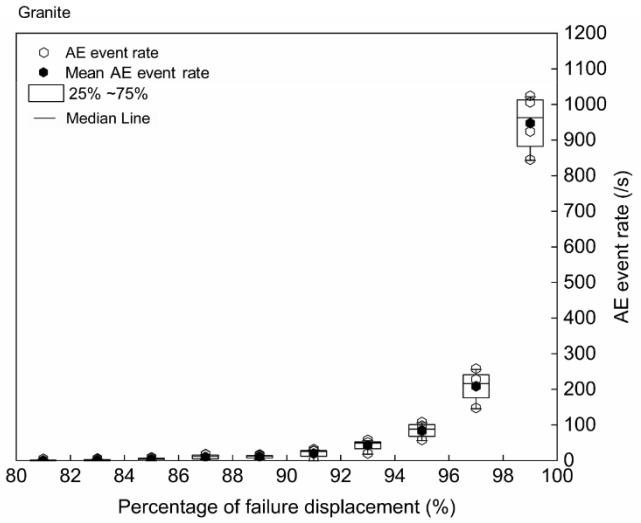
Granite
AE event rate
Mean AE event rate
25% ~75%
Median Line
AE event rate (/s)
Percentage of failure displacement (%)

(a)

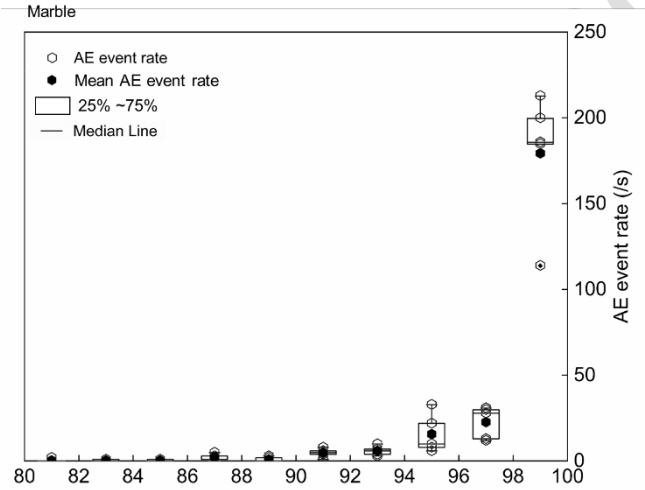
Marble
AE event rate
Mean AE event rate
25% ~75%
Median Line
AE event rate (/s)

(b)

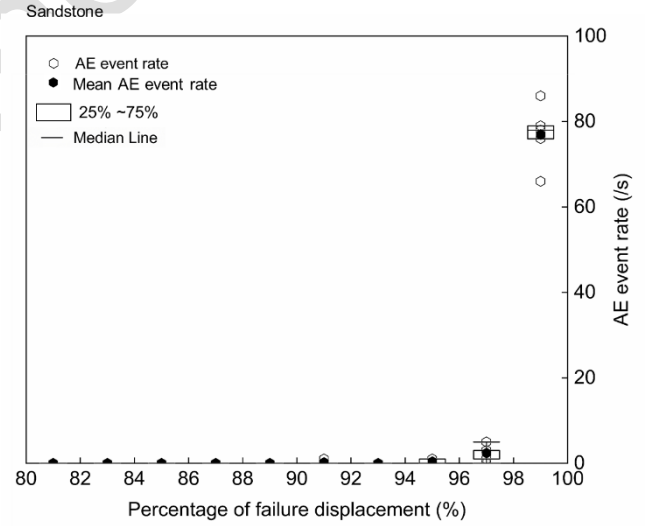
Sandstone
AE event rate
Mean AE event rate
25% ~75%
Median Line
AE event rate (/s)
Percentage of failure displacement (%)

(c)

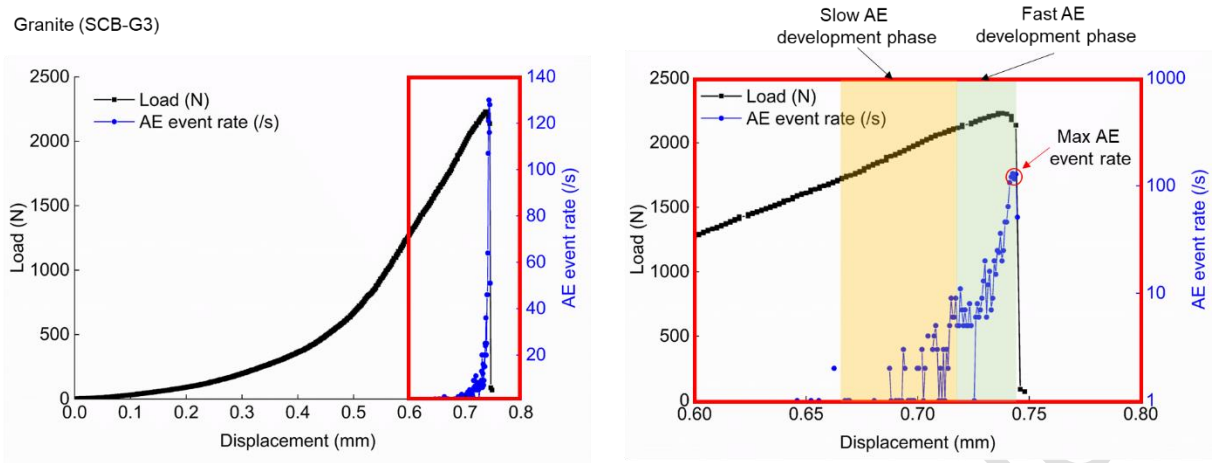

(d)

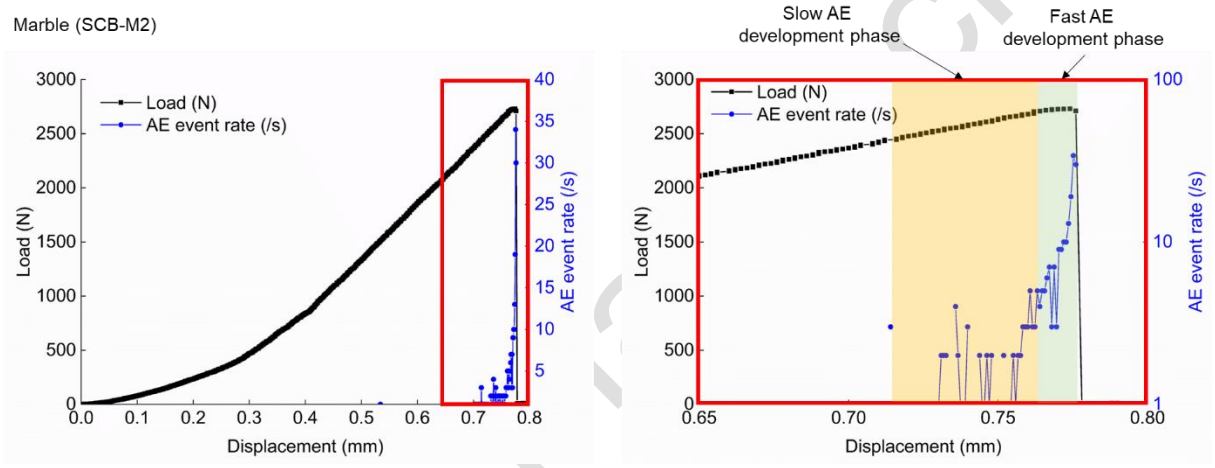

(e)

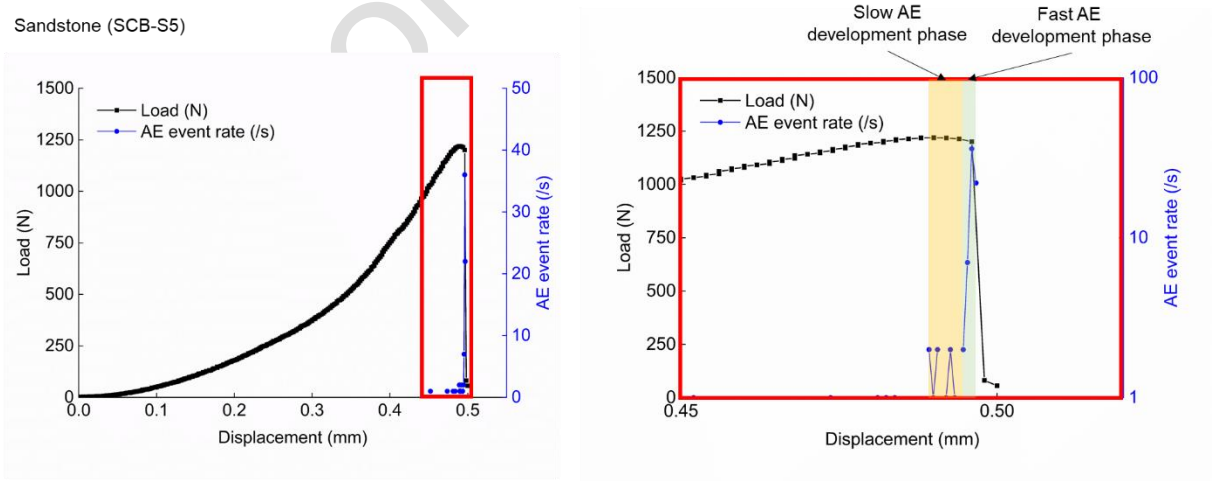

(f)

Fig. 5 Variations of AE event rate with the normalized displacement of all the tested (a) granite, (b) marble and (c) sandstone specimens. Only the variations when normalized displacement is larger than the 80 % of failure displacement are presented because few AE events are detected before this point. Typical variations of load and AE event rate with displacement for the (d) granite (SCB-G3), (e) marble (SCB-M2) and (f) sandstone (SCB-S5)

764 specimens in the SCB tests. The figures in (d), (e) and (f) on the right side are the zoom-in view of the red
765 rectangular portion in the figures on the left side. (Colorful online)

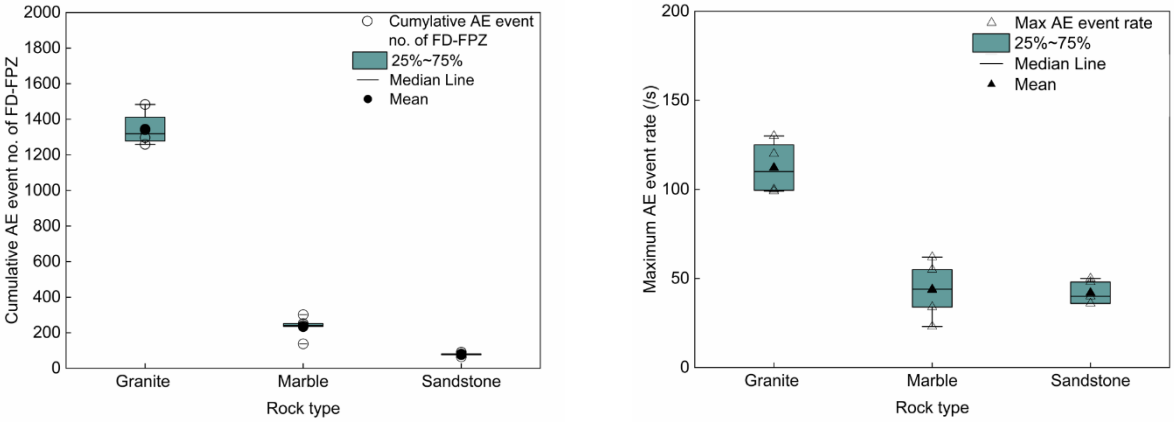

(a) (b)

Fig. 6 The scatter and box plots of the (a) maximum AE event rates and (b) cumulative AE event numbers preceding the initiation of macrocracks for all the granite, marble and sandstone specimens in the SCB tests

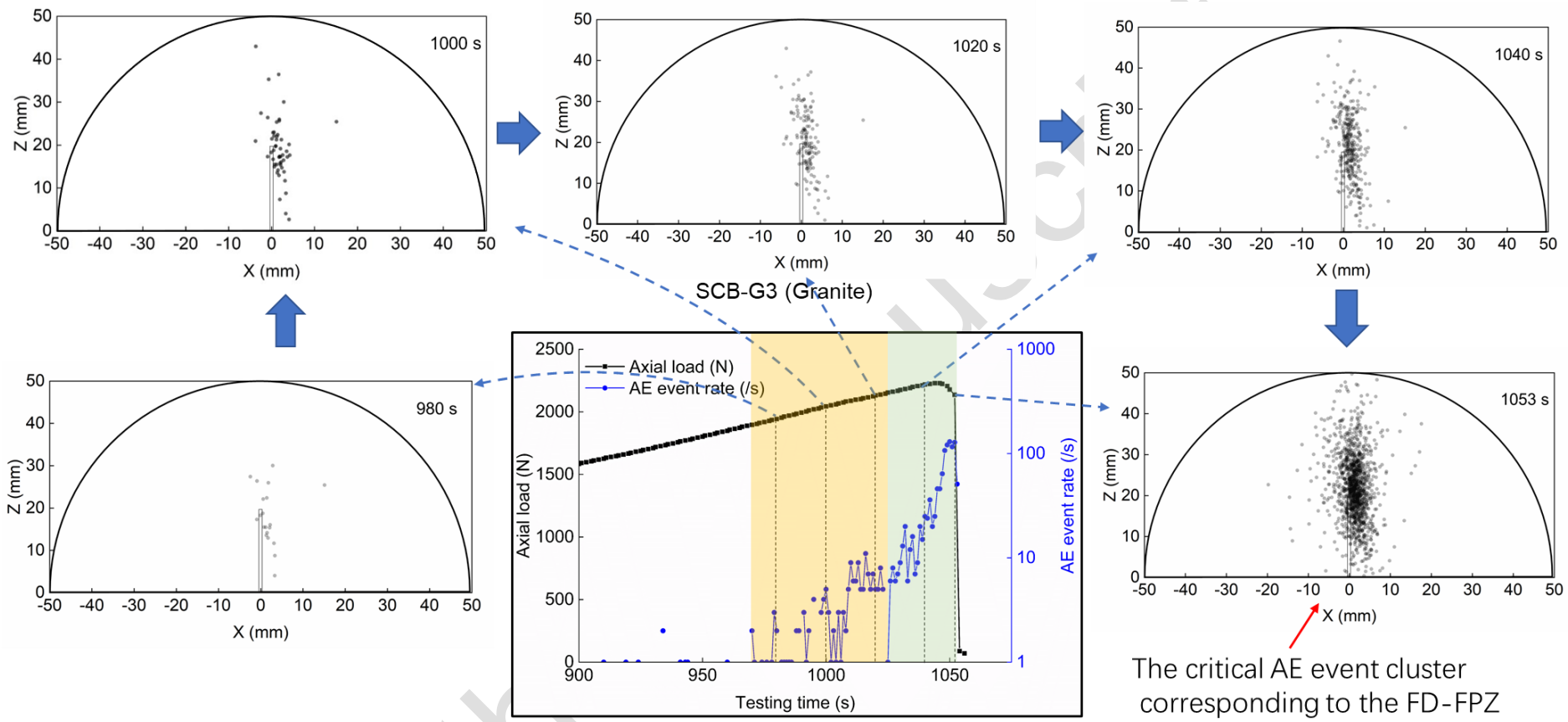
1000 s
1020 s
1040 s
980 s
1053 s
Z (mm)
X (mm)
SCB-G3 (Granite)
Axial load (N)
AE event rate (/s)
Testing time (s)
The critical AE event cluster
corresponding to the FD-FPZ

(a)

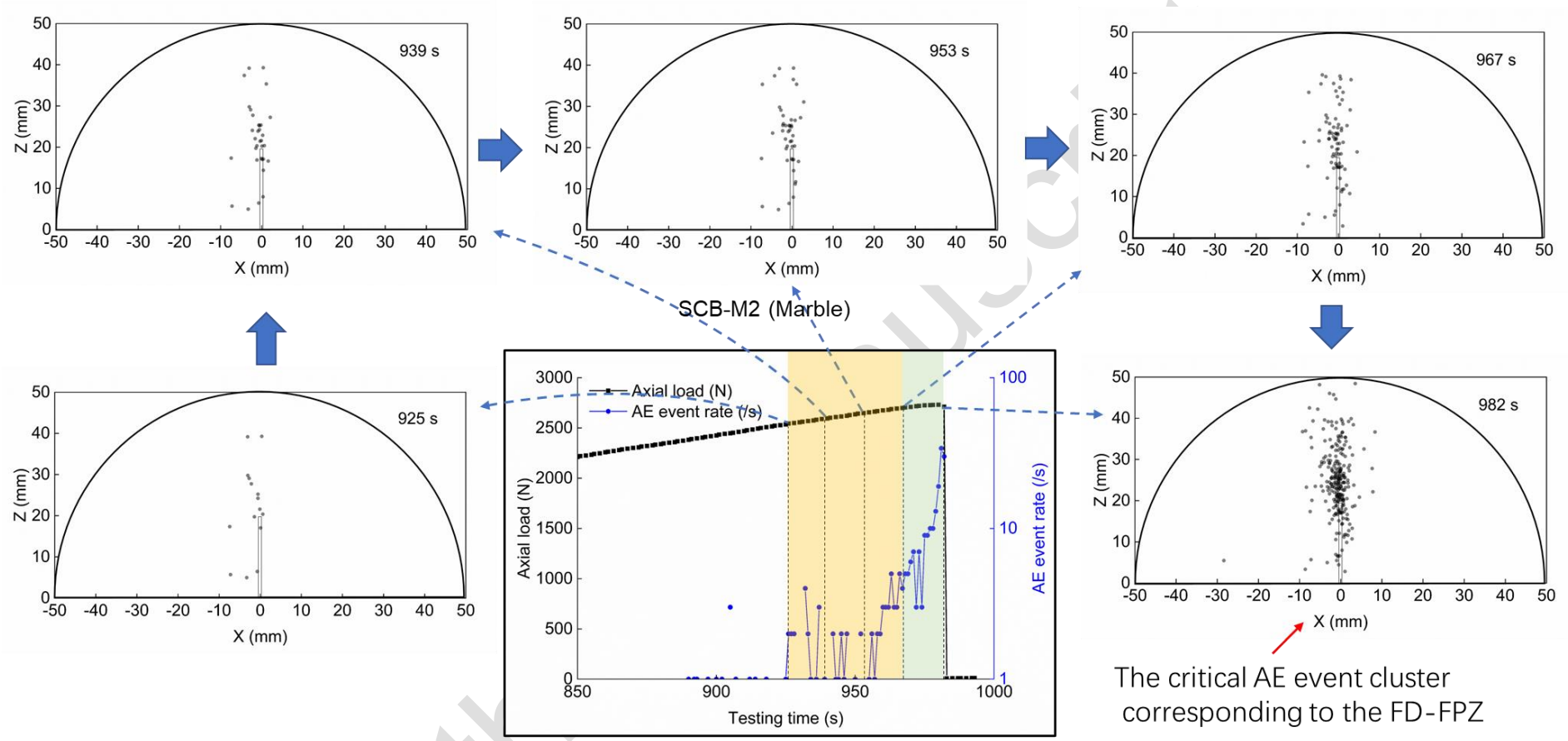
939 s
953 s
967 s
925 s
982 s
Z (mm)
X (mm)
SCB-M2 (Marble)
Axial load (N)
AE event rate (/s)
Testing time (s)
The critical AE event cluster
corresponding to the FD-FPZ

(b)

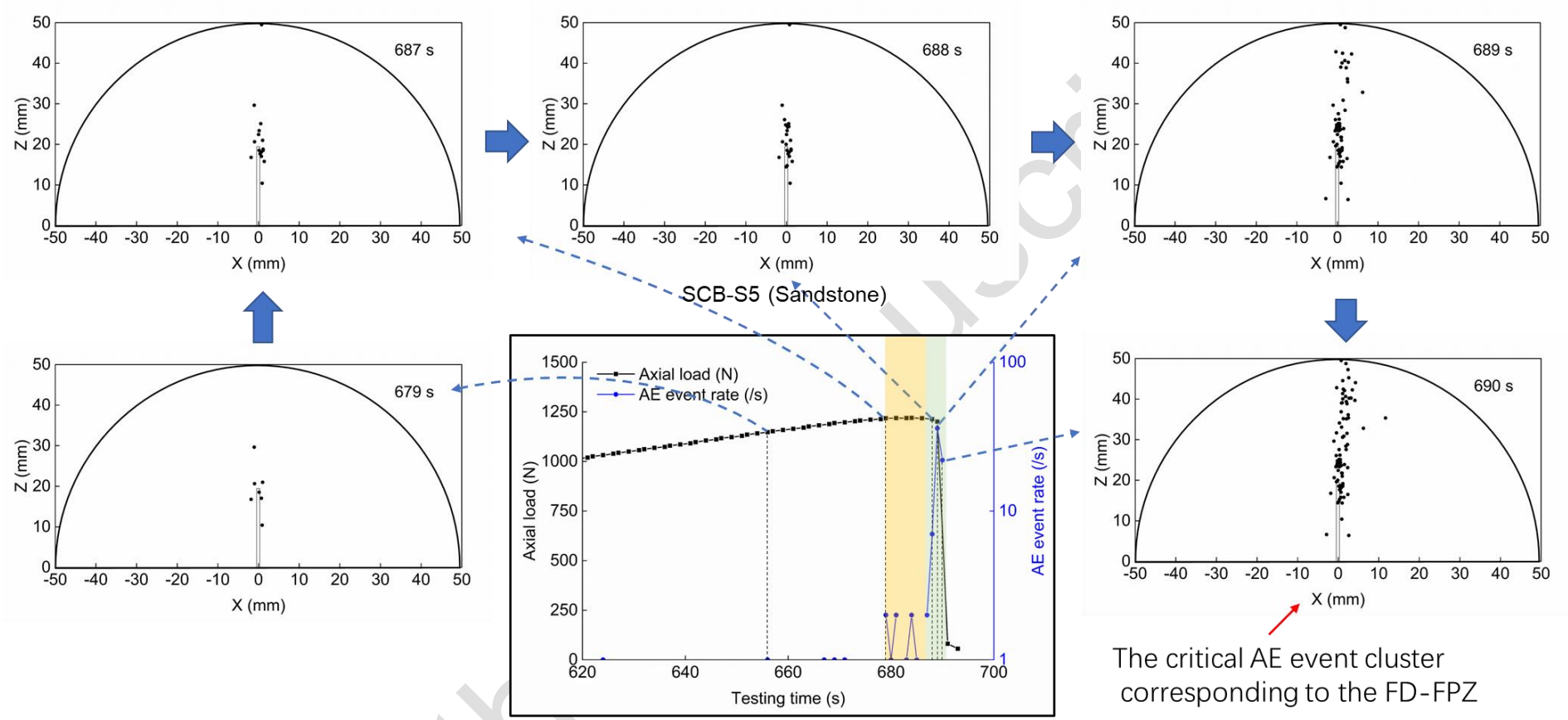

(c)

Fig. 7 The spatial-temporal evolution features of AE events in the SCB tests on specimens (a) SCB-G3, (b) SCB-M2, (c) SCB-S5. In the scatter plots, the cumulative AE events (black dots) are projected on the XOZ plane (refer to Fig. 2b). The semi-circulars denote the boundary of the SCB specimens. The rectangles in the center of the semi-circulars denote the pre-existing notches

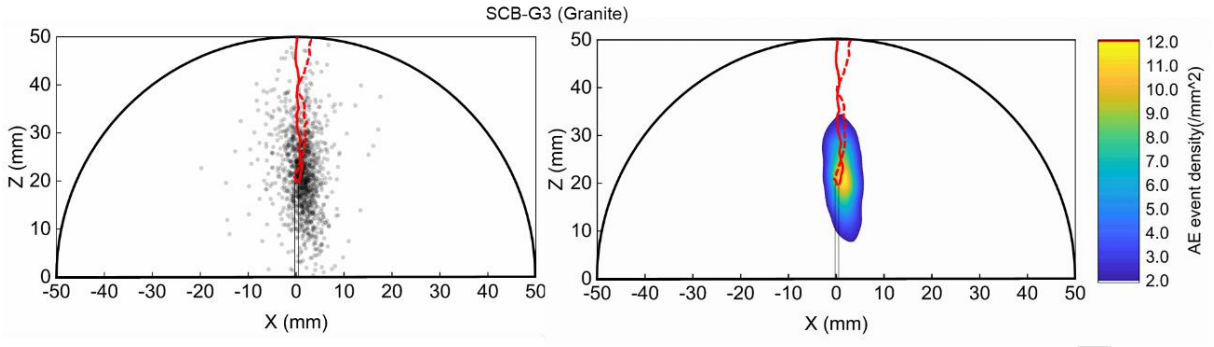
SCB-G3 (Granite)
Z (mm)
X (mm)
AE event density(/mm^2)
12.0
11.0
10.0
9.0
8.0
7.0
6.0
5.0
4.0
3.0
2.0

(a)

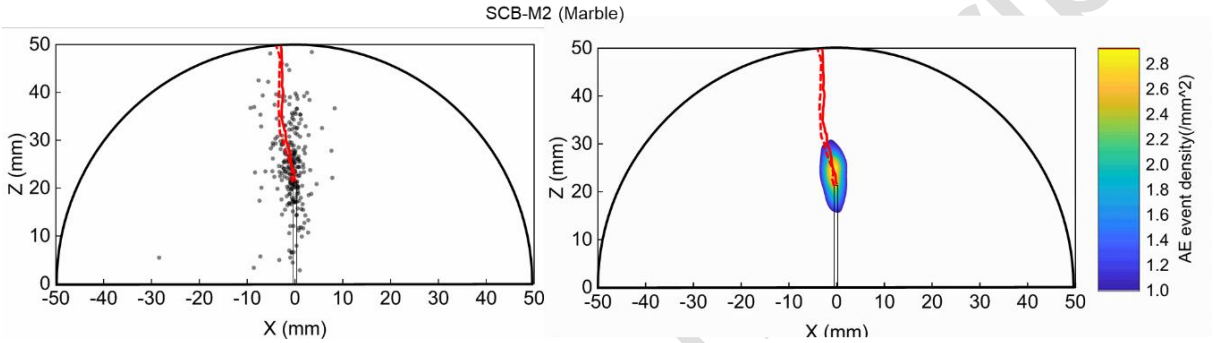
SCB-M2 (Marble)
Z (mm)
X (mm)
AE event density(/mm^2)
2.8
2.6
2.4
2.2
2.0
1.8
1.6
1.4
1.2
1.0

(b)

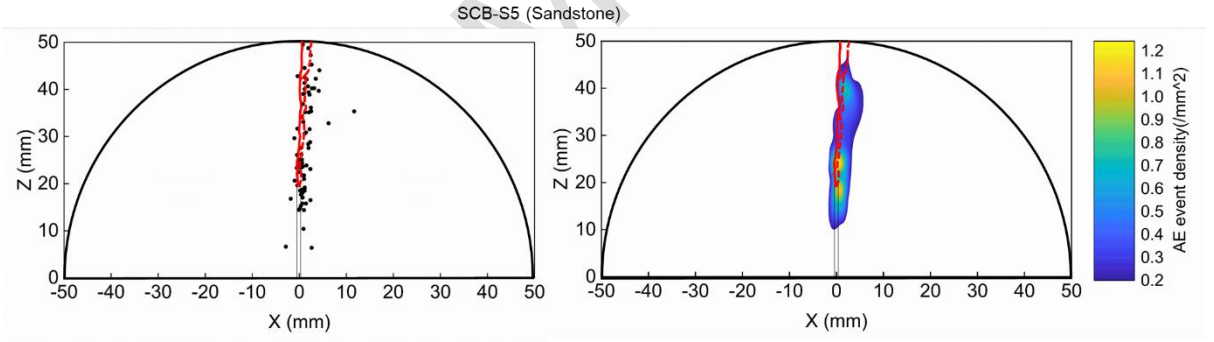
SCB-S5 (Sandstone)
Z (mm)
X (mm)
AE event density(/mm^2)
1.2
1.1
1.0
0.9
0.8
0.7
0.6
0.5
0.4
0.3
0.2

(c)

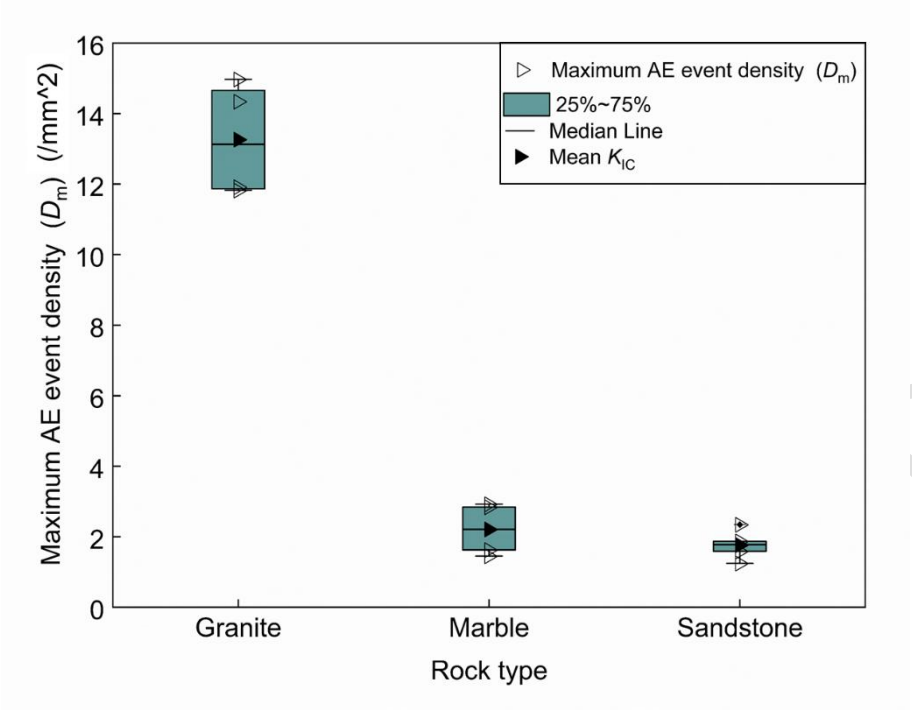

(d)

Fig. 8 The scatter and event density contour plots of the critical AE event clusters specimens (a) SCB-G3 (granite), (b) SCB-M2 (marble) and (c) SCB-S5 (sandstone) from the front view (XOZ). The contour thresholds are set to be 2 mm^{-2}, 1 mm^{-2}, 0.2 mm^{-2} for specimens SCB-G3, SCB-M2, SCB-S5, respectively. The dots are the AE events. The red solid and dotted lines are the macrocrack paths on the front and back surfaces of the SCB specimens, respectively. (d) The scatter and box plots of the maximum AE event density (Colorful online)

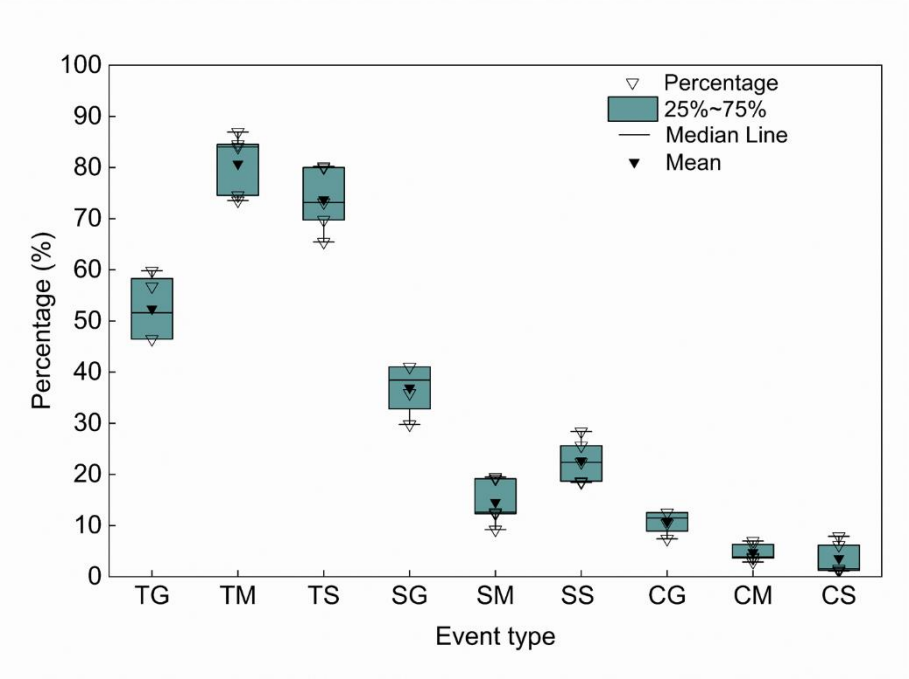

800

801 **Fig. 9** Percentages of tensile, shear and collapse events constituting the critical AE event clusters of
802 SCB granite, marble, and sandstone specimens. The meanings of tick labels of X-axis: tensile event in
803 the granite (TG), marble (TM) and sandstone (TS) specimens; shear event in the granite (SG), marble
804 (SM), and sandstone (SS) specimens; collapse event in the granite (CG), marble (CM) and sandstone
805 (CS) specimens

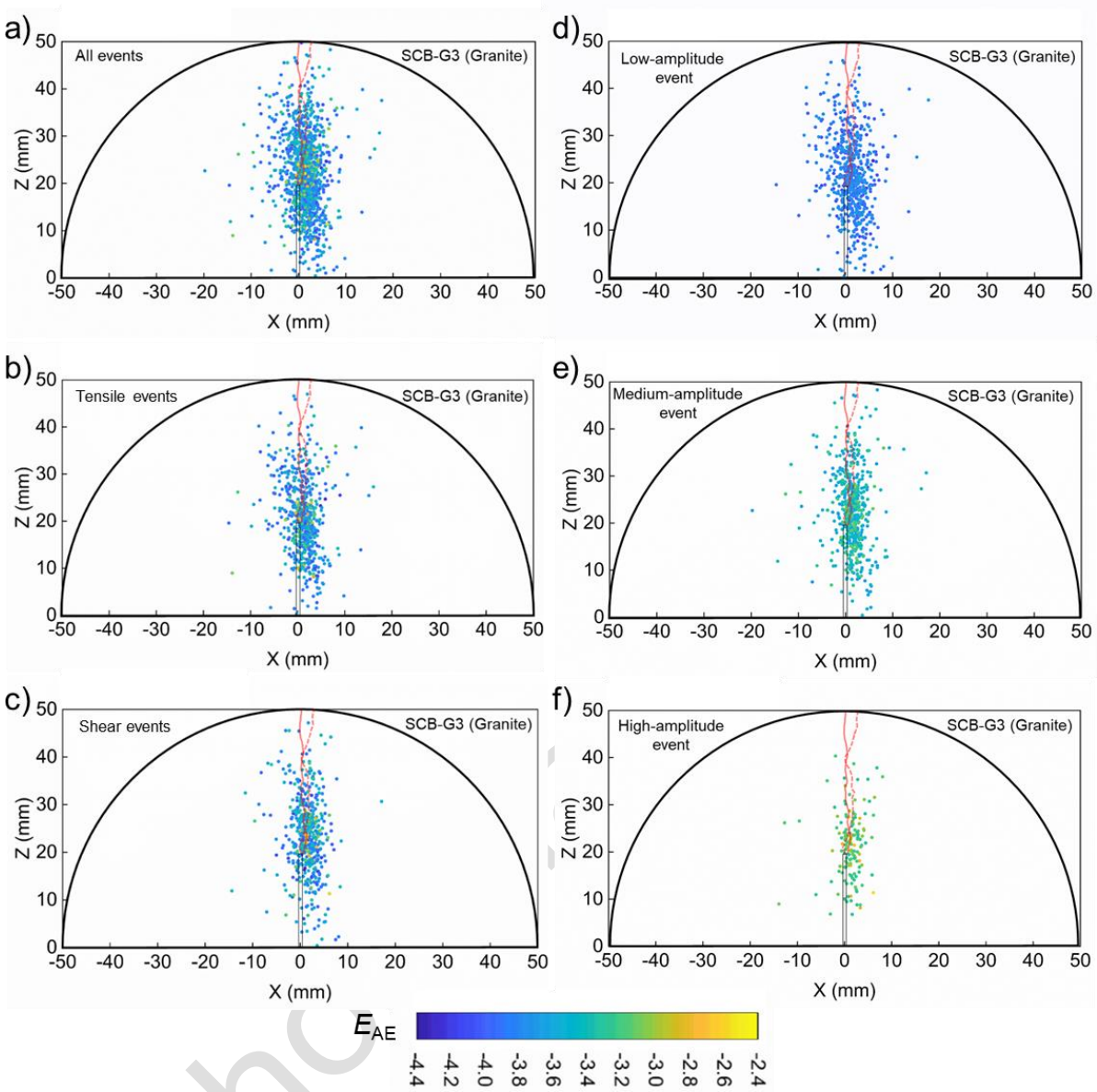

806

807 **Fig. 10** The scatter diagram of (a) all the AE events, (b) tensile AE events, (c) shear AE events, (d) low-
808 amplitude events ($-4.4 < E_{AE} \leq -3.7$), (e) medium-amplitude events ($-3.7 < E_{AE} \leq -3.1$), and (f) (d) high-
809 amplitude events ($-3.1 < E_{AE} \leq -2.4$), with different relative amplitude (E_{AE}) constituting the critical AE
810 event cluster in the SCB test on granite specimen SCB-G3

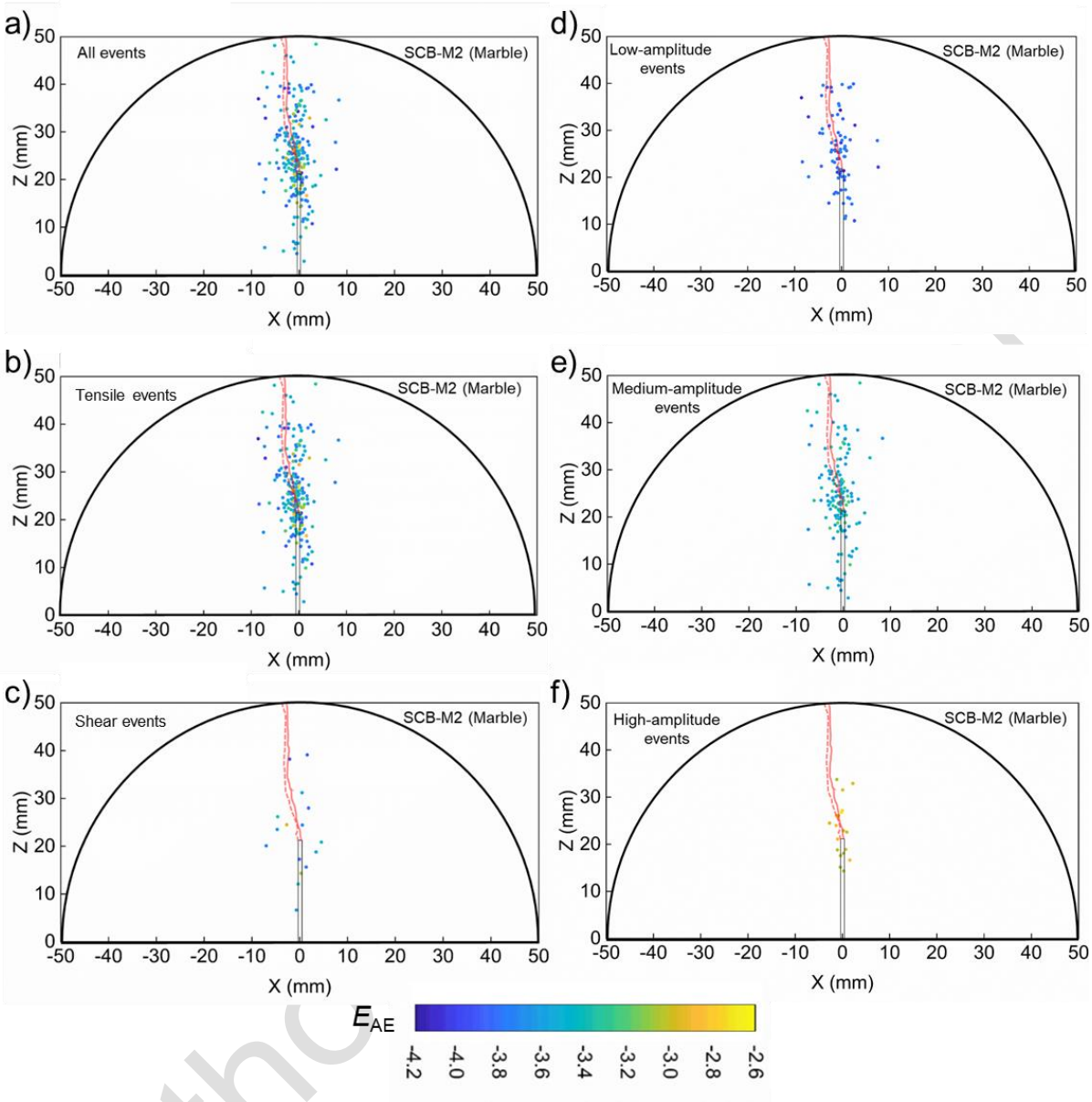

811

812 **Fig. 11** The scatter diagram of (a) all the AE events, (b) tensile AE events, (c) shear AE events, (d) low-
813 amplitude events ($-4.2 < E_{AE} \leq -3.7$), (e) medium-amplitude events ($-3.7 < E_{AE} \leq -3.1$), and (f) (d) high-
814 amplitude events ($-3.1 < E_{AE} \leq -2.6$), with different relative amplitude (E_{AE}) constituting the critical AE
815 event cluster in the SCB test on granite specimen SCB-M2

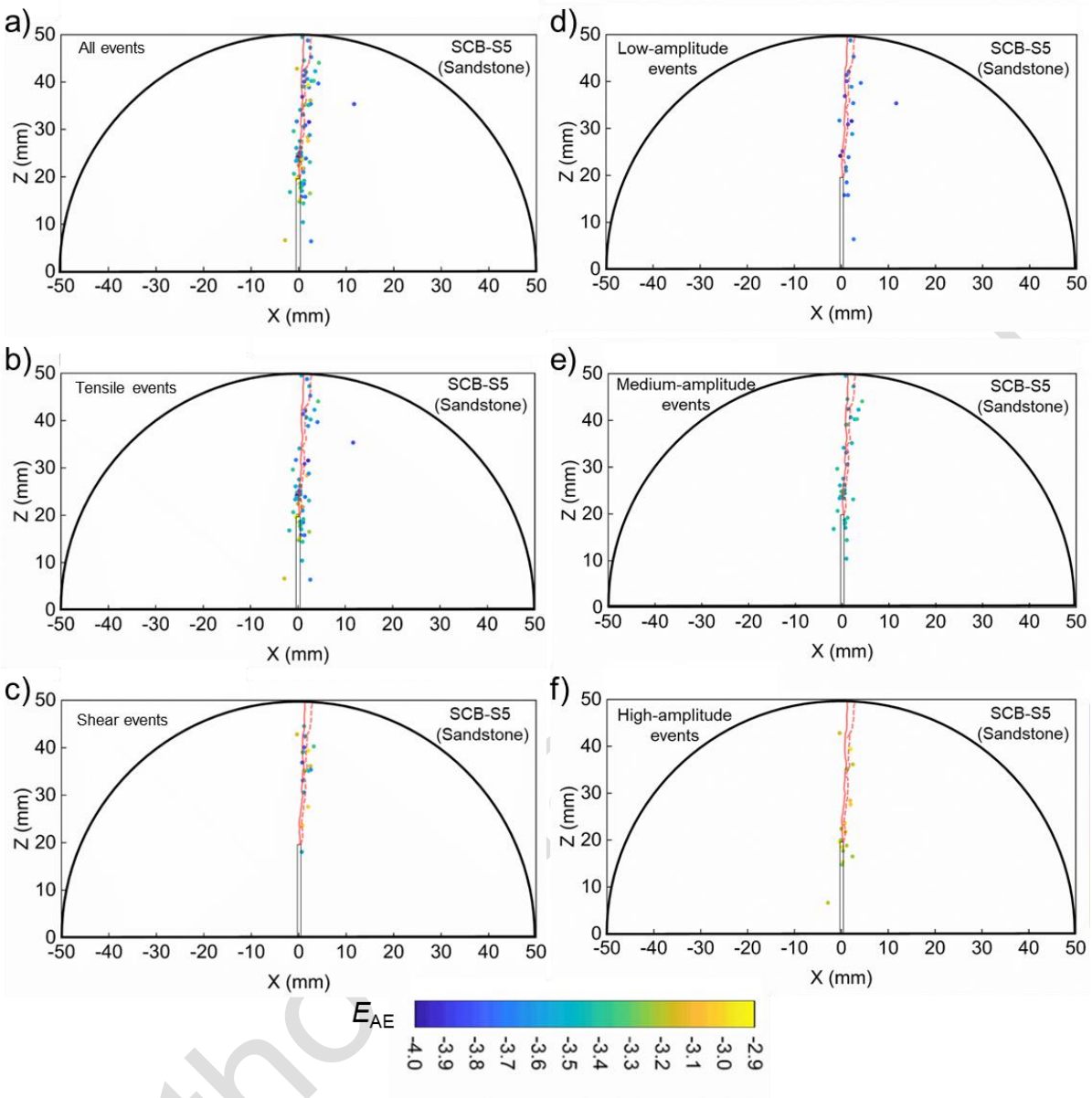

Fig. 12 The scatter diagram of (a) all the AE events, (b) tensile AE events, (c) shear AE events, (d) low-amplitude events ($-4 < E_{AE} \leq -3.6$), (e) medium-amplitude events ($-3.6 < E_{AE} \leq -3.3$), and (f) (d) high-amplitude events ($-3.3 < E_{AE} \leq -2.9$), with different relative amplitude (E_{AE}) constituting the critical AE event cluster in the SCB test on granite specimen SCB-S5

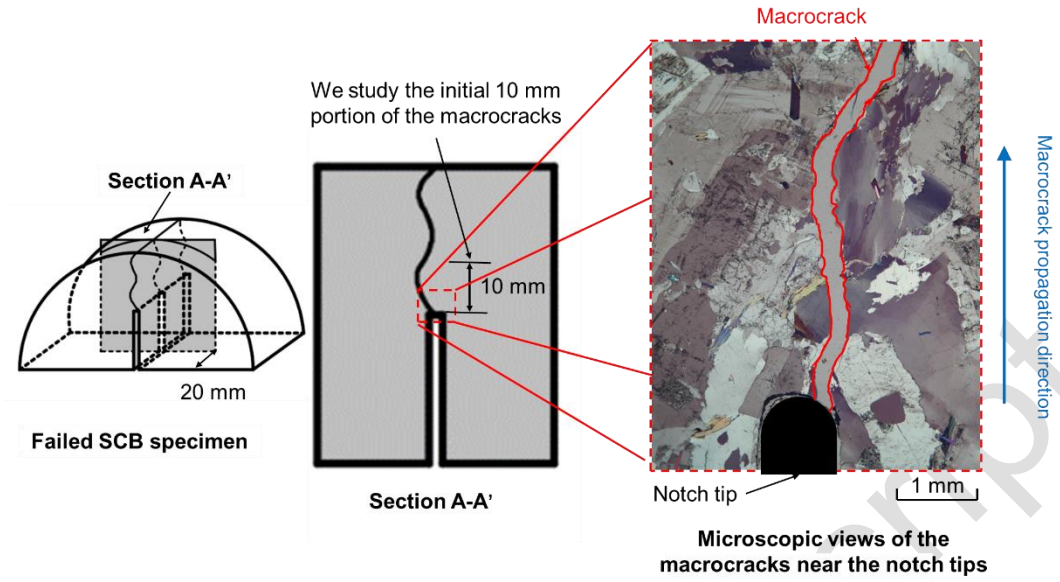

821

822 (a)

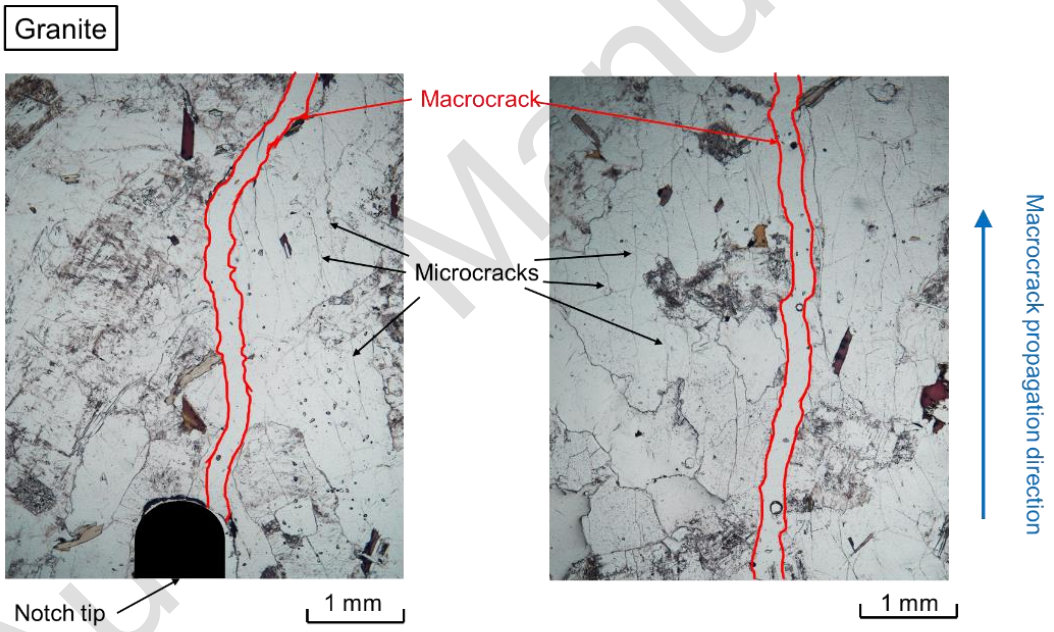

823

824 (b)

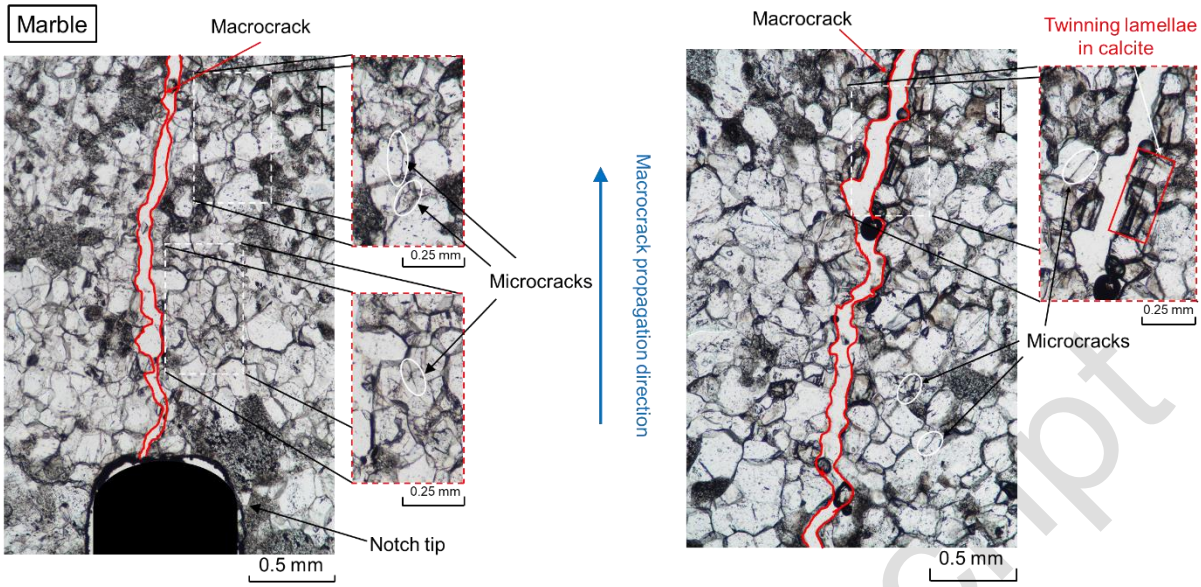

(c)

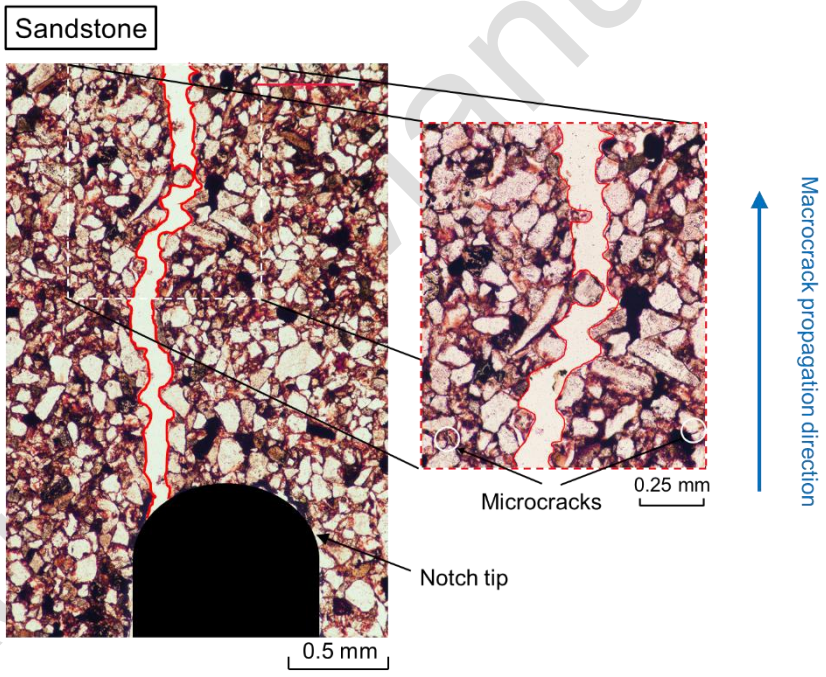

(d)

Fig. 13 (a) The locations of thin-section samples in the failed SCB specimen and the area where we conduct the microscopic analysis. The microscopic views of the macrocrack near the notch tips in the thin-section samples of (b) granite under both XPL and PPL, (c) marble under PPL and (d) sandstone under PPL.

Confidential manuscript submitted to Rock Mechanics and Rock Engineering

Supplementary material for

Acoustic emission characteristics during the microcracking processes of granite, marble and sandstone under mode I loading

Tian Yang Guo, Qi Zhao*

Department of Civil and Environmental Engineering, The Hong Kong Polytechnic University, Hong Kong, China

Contents of this file

Figures S1 to S5

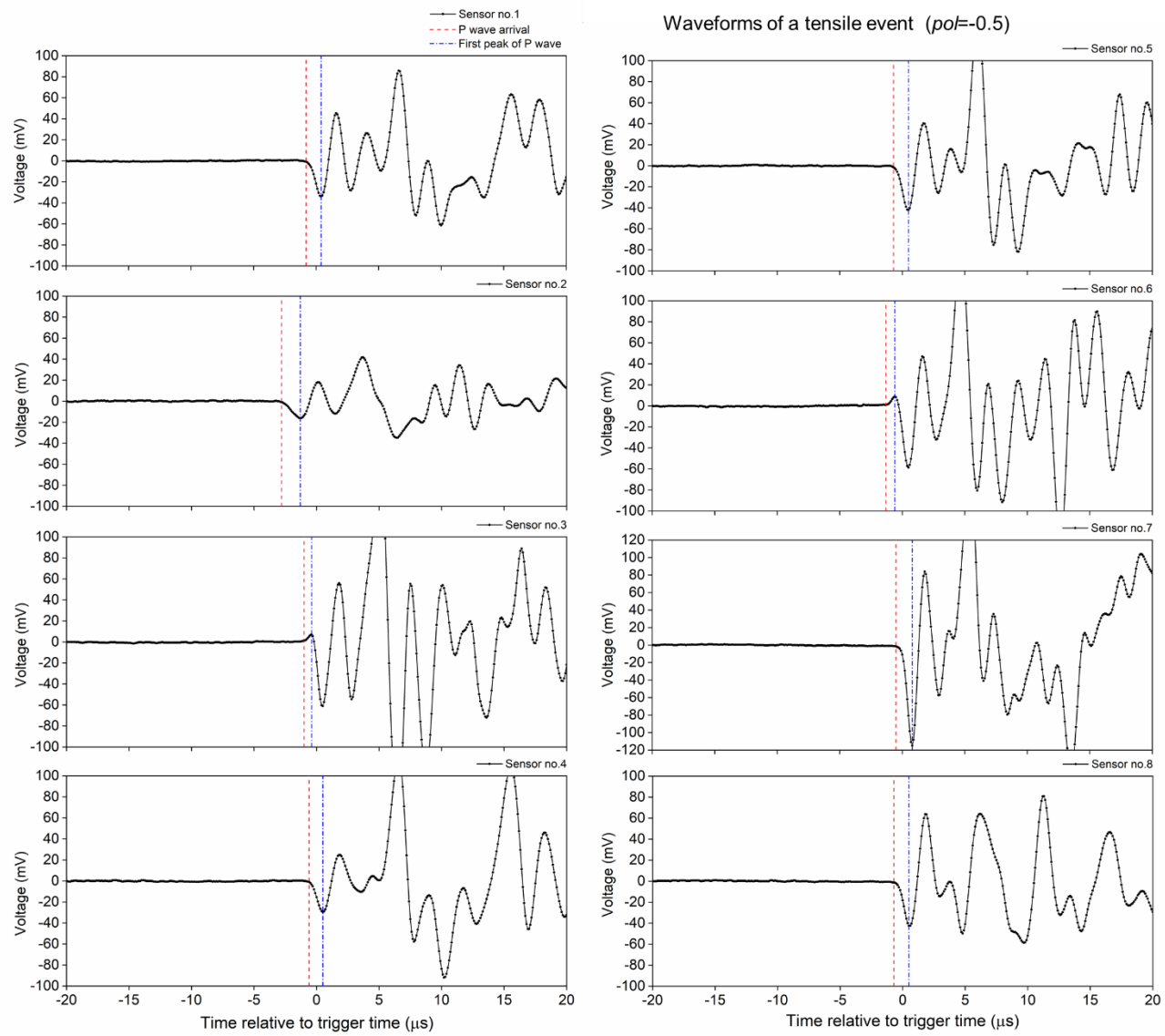

845

846 (a)

847

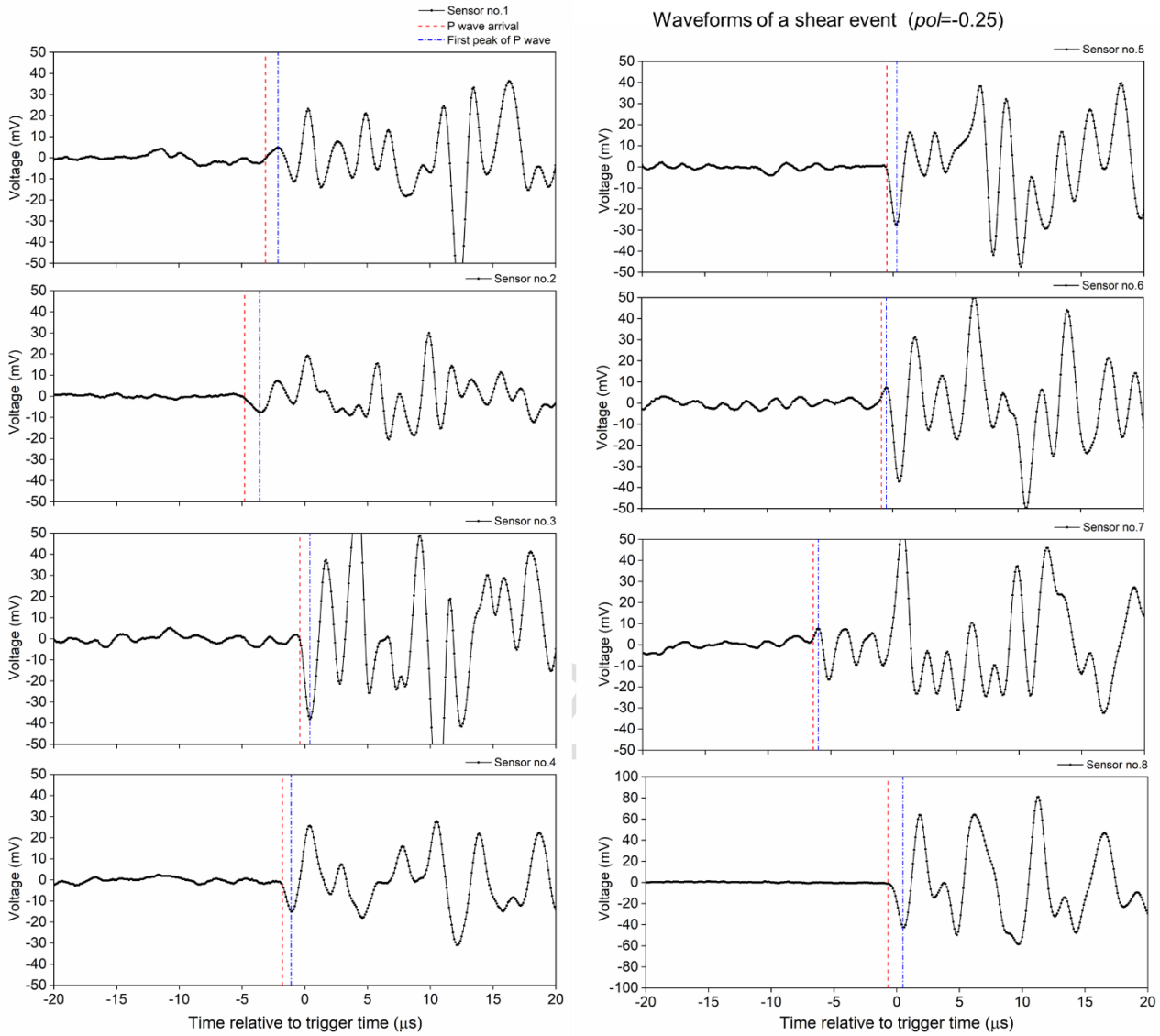

848

849 (b)

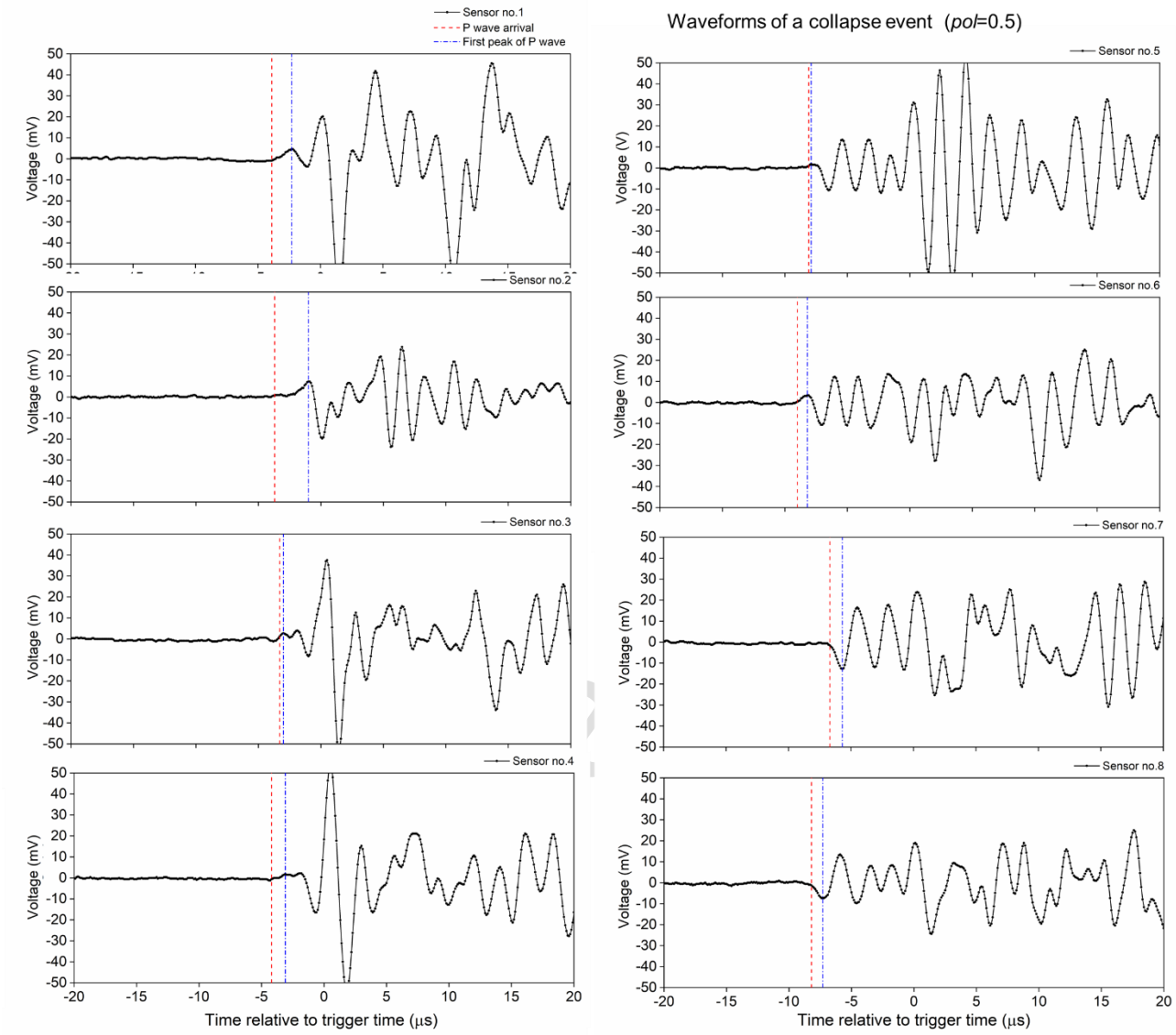

(c)

Figure S1. The P wave arrival picked by the Akaike Information Criterion (AIC) picker (red dotted line) and the first peak of P wave (blue dotted line) of the AE waveforms of (a) tensile, (b) shear and (c) collapse events.

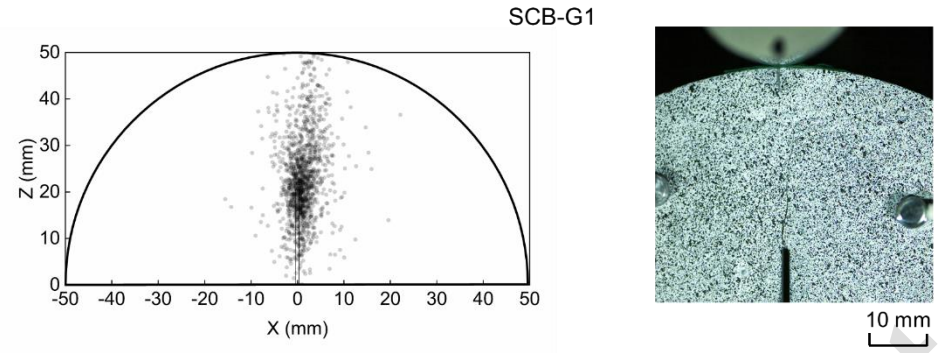

(a)

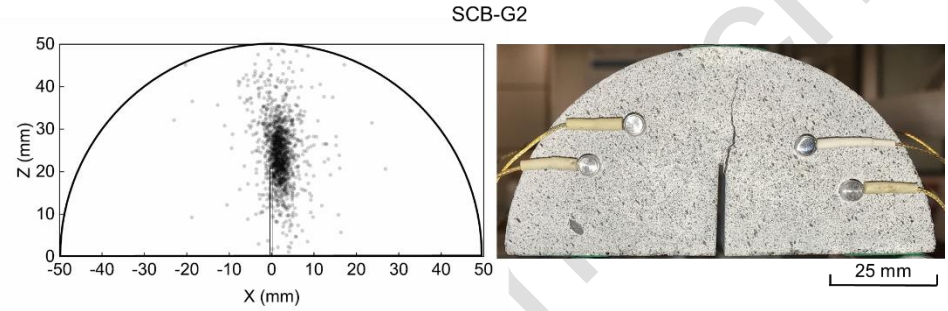

(b)

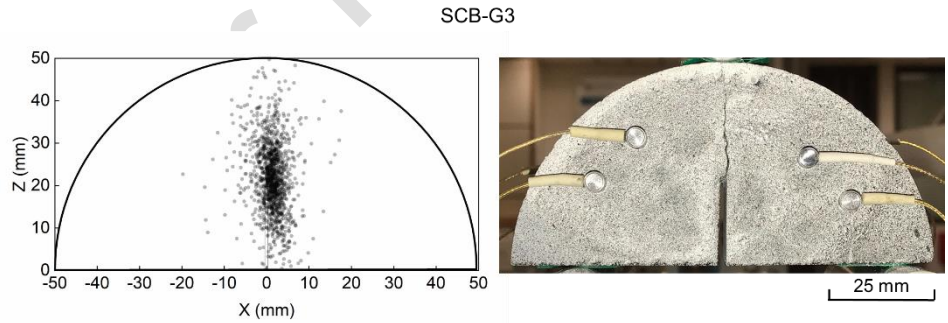

(c)

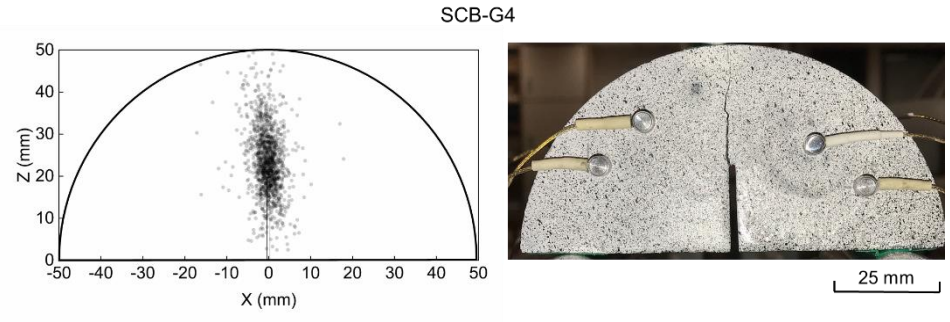

(d)

Figure S2. The scatter plots of AE events corresponding to the fully-developed fracture process zone of SCB granite specimens and the specimen photos after failure: (a) SCB-G1, (b) SCB-G2, (c) SCB-G3, (d) SCB-G4 Please note that the front surfaces of the specimens have been sprayed with speckles for another study.

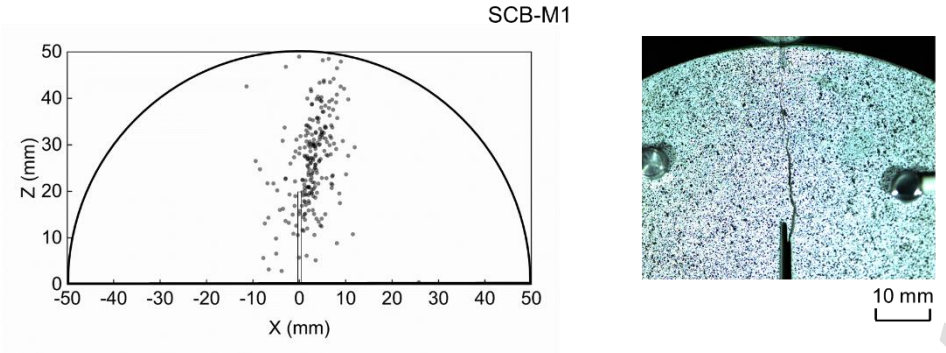

872

873 (a)

874

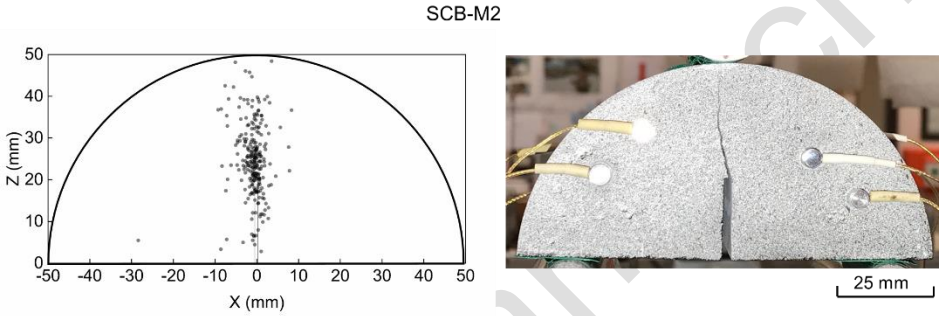

875

876 (b)

877

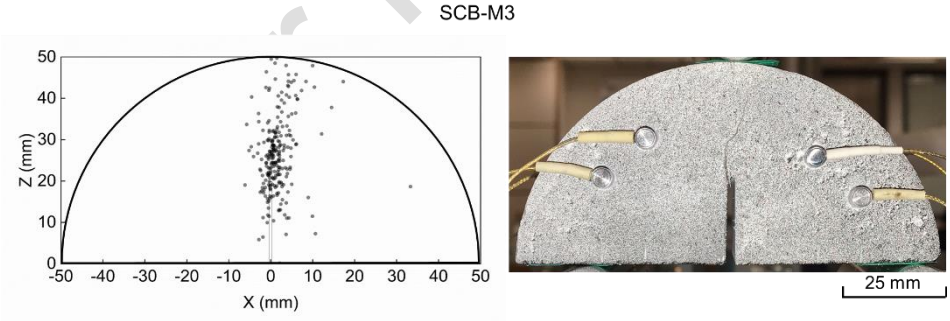

878

879 (c)

880

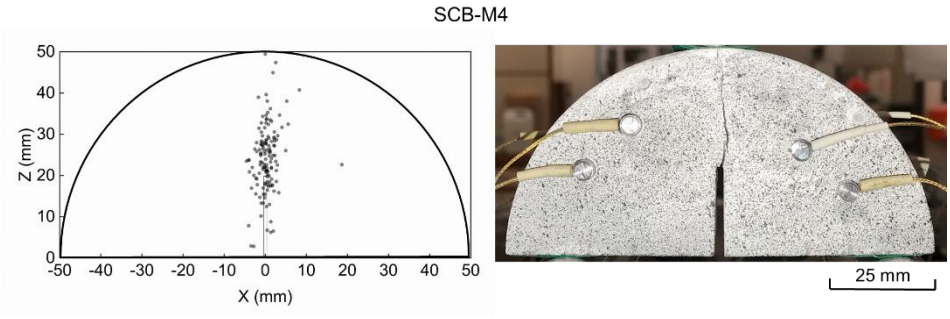

(d)

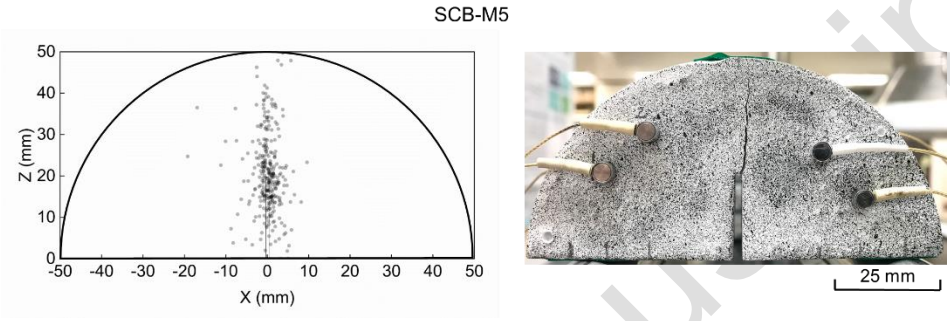

(e)

Figure S3. The scatter plots of AE events corresponding to the fully-developed fracture process zone of SCB marble specimens and the photos of the front surface of the specimens after failure: (a) SCB-M1, (b) SCB-M2, (c) SCB-M3, (d) SCB-M4, (e) SCB-M5. Please note that the front surfaces of the specimens have been sprayed with speckles for another study.

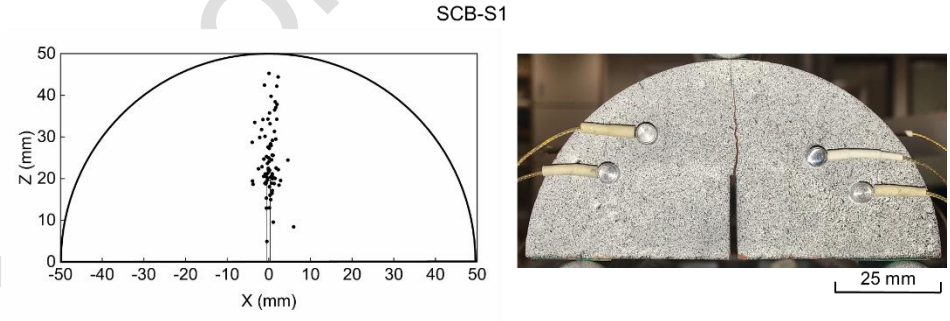

(a)

SCB-S2

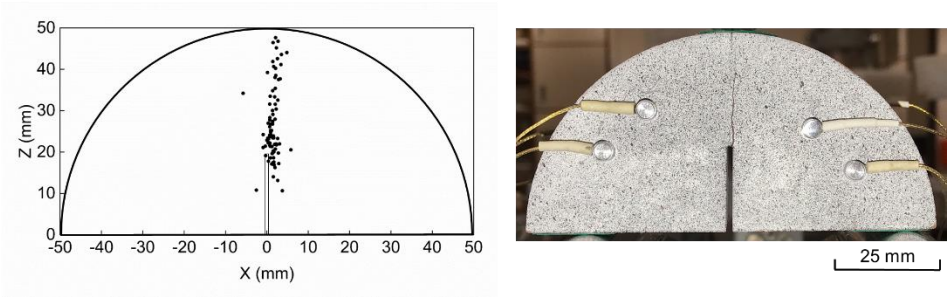

(b)

SCB-S3

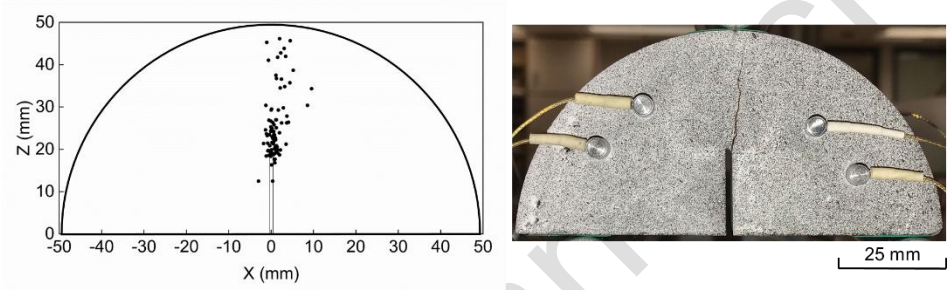

(c)

SCB-S4

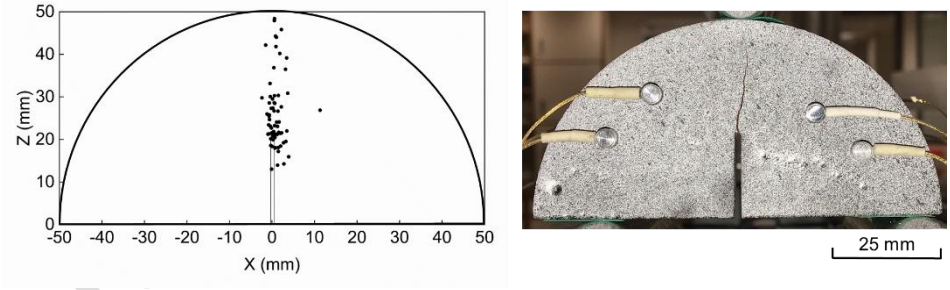

(d)

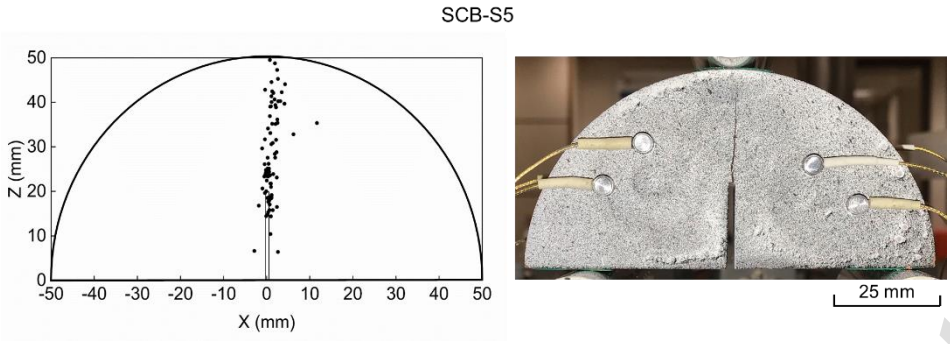

(e)

Figure S4. The scatter plots of AE events corresponding to the fully-developed fracture process zone of SCB marble specimens and the photos of the front surface of the specimens after failure: (a) SCB-M1, (b) SCB-M2, (c) SCB-M3, (d) SCB-M4, (e) SCB-M5. Please note that the front surfaces of the specimens have been sprayed with speckles for another study.

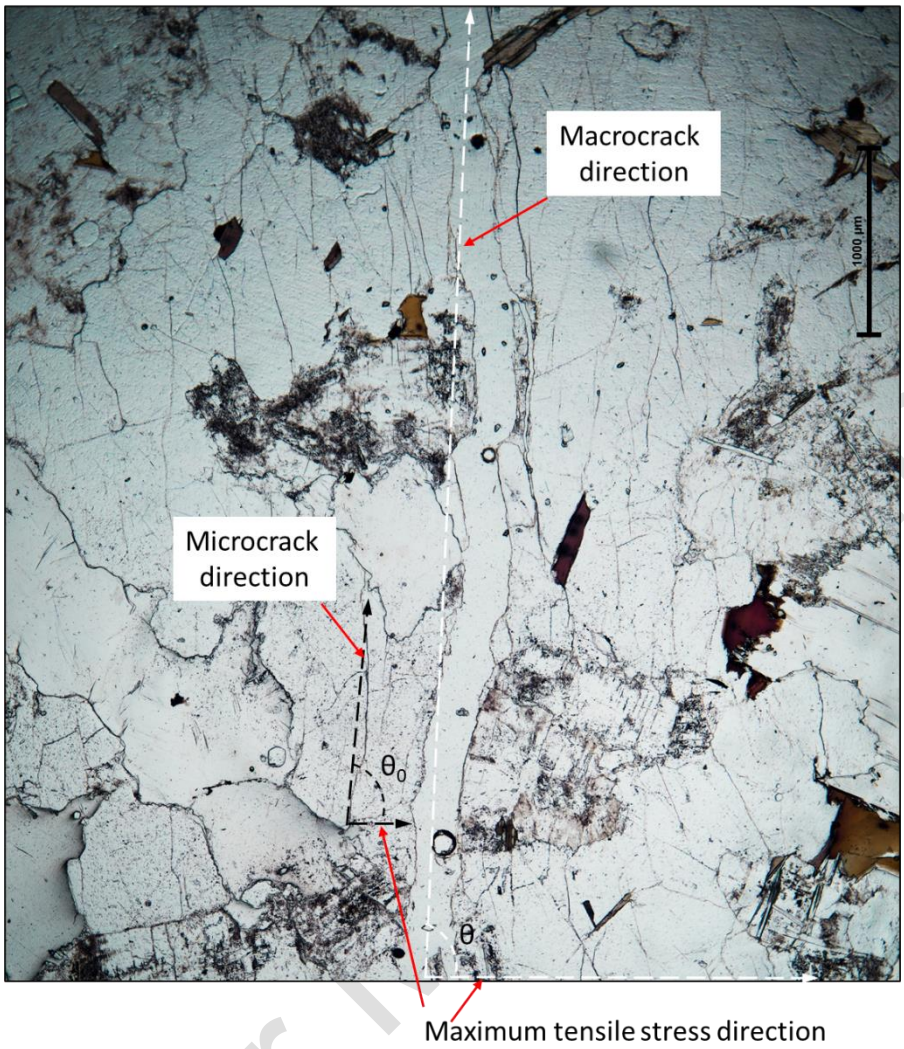

(a)

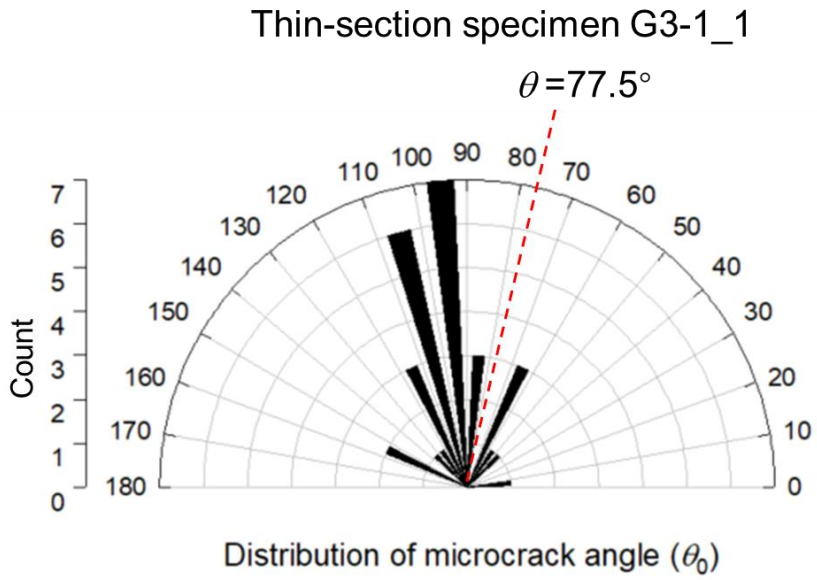

(b)

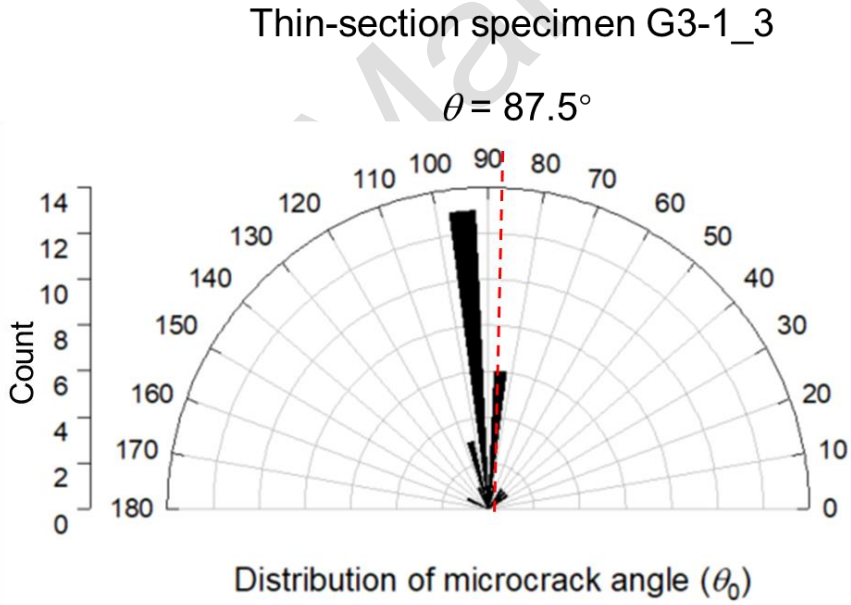

(c)

Figure S5. (a) Illustration of quantitative thin-section analysis. Microcrack angle (θ_0) is defined as the angle between the direction of microcrack direction and that of maximum tensile stress. Macrocrack angle (θ) is defined as the angle between the direction of macrocrack direction and that of maximum tensile stress. Thin section analysis results of thin-section specimens (b) G3-1_1 and (c) G3-1_3. The results show that most of the microcracks are subparallel to the macrocrack.